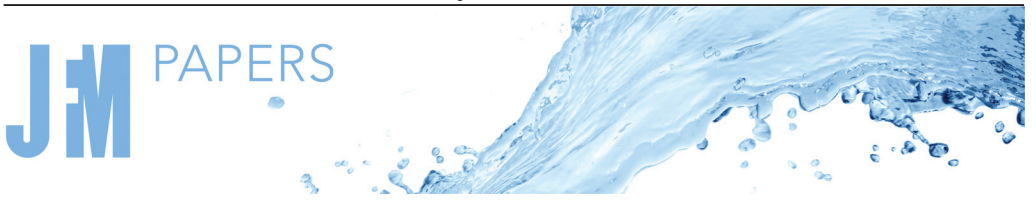
J. Fluid Mech. (2022), *vol*. 934, A42, doi:10.1017/jfm.2021.1121



Near-onset dynamics in natural doubly diffusive convection

Cédric Beaume[1],†**, Alastair M. Rucklidge**[1] **and Joanna Tumelty**[1]

[1]School of Mathematics, University of Leeds, Leeds LS2 9JT, UK

(Received 10 August 2021; revised 2 November 2021; accepted 9 December 2021)

Doubly diffusive convection is considered in a vertical slot where horizontal temperature and solutal variations provide competing effects to the fluid density while allowing the existence of a conduction state. In this configuration, the linear stability of the conductive state is known, but the convection patterns arising from the primary instability have only been studied for specific parameter values. We have extended this by determining the nature of the primary bifurcation for all values of the Lewis and Prandtl numbers using a weakly nonlinear analysis. The resulting convection branches are extended using numerical continuation and we find large-amplitude steady convection states can coexist with the stable conduction state for sub- and supercritical primary bifurcations. The stability of the convection states is investigated and attracting travelling waves and periodic orbits are identified using time stepping when these steady states are unstable.

Key words: double diffusive convection, bifurcation

1. Introduction

Doubly diffusive convection can occur when a binary fluid is subject to external gradients of temperature and of concentration. It has primarily been studied in the context of oceanography as an important mechanism for heat and salt transport (Huppert & Turner 1981; Schmitt 1994), since approximately 44 % of the world's oceans are known to display this phenomenon (You 2002). Doubly diffusive convection can display a wealth of behaviour that depends on the respective orientations of the (thermal and solutal) driving gradients. At low latitude, oceans typically feature thermohaline staircases (Schmitt *et al.* 1987, 2005), where the flow is characterised by well-mixed horizontal layers interspersed with interfaces displaying sharp upward pointing gradients of temperature and salinity. In configurations forced by upward gradients of salinity and temperature, fluids display strikingly complex dynamics characterised by an alternation of well-mixed convection zones and fingers transporting salt mostly vertically (Krishnamurti 2003, 2009).

† Email address for correspondence: c.m.l.beaume@leeds.ac.uk

© The Author(s), 2022. Published by Cambridge University Press

https://doi.org/10.1017/jfm.2021.1121 Published online by Cambridge University Press

This salt fingering instability is a natural mechanism that enhances the local mixing of the oceans (Schmitt 1994). At high latitude, the forcing gradients typically point downwards and perturbations to the thermohaline staircase give rise to oscillatory dynamics in a behaviour called diffusive layering (Kelley *et al.* 2003; Pérez-Santos *et al.* 2014). Similar doubly diffusive phenomena are also found at the Earth's core–mantle boundary (Lay, Hernlund & Buffett 2008), in astrophysical flows (Spiegel 1969, 1972; Bethe 1990) and in processes involving solidification (Wilcox 1993), such as in magma crystallisation (Huppert & Sparks 1984).

Originally motivated by the above configurations, doubly diffusive convection has become a paradigm for the study of fluids as dynamical systems. A large variety of flow states comprised of convection rolls have been identified, including standing, travelling and modulated waves (Deane, Knobloch & Toomre 1988; Kolodner 1991; Predtechensky *et al.* 1994). Temporal complexity has also been found in various forms (Spina, Toomre & Knobloch 1998; Batiste *et al.* 2001) and is generated in a number of ways (Knobloch *et al.* 1986; Rucklidge 1992; Beaume 2020). Work focusing on the steady state dynamics also revealed intricate phenomena like spatial localisation in the presence (Mercader *et al.* 2009, 2011) and in absence (Beaume, Bergeon & Knobloch 2011) of the Soret effect. Localised convection states, called convectons, are found on solution branches exhibiting oscillatory trajectories in parameter space in a behaviour called snaking (Knobloch 2015). Travelling versions of convectons have also been found and produce an interesting hierarchy of interconnected instabilities (Watanabe, Iima & Nishiura 2012, 2016).

Practical considerations led to the study of inclined domains, where gravity and the driving gradients are no longer aligned (Paliwal & Chen 1980*a*,*b*; Bergeon, Ghorayeb & Mojtabi 1999), as well as cases in which the salinity and temperature gradients are not aligned with each other (Tsitverblit & Kit 1993; Tsitverblit 1995; Dijkstra & Kranenborg 1996). Motivated by solidification fronts (Wilcox 1993) and mixing currents in the vicinity of icebergs (Huppert & Turner 1981), this article focuses on a configuration, typically referred to as natural doubly diffusive convection, where the driving gradients are aligned but orthogonal to gravity.

The bifurcation scenario for a range of small-aspect-ratio domains was elucidated by Xin, Le Quéré & Tuckerman (1998) and Bergeon & Knobloch (2002), and large-aspect-ratio domains were found to support the existence of spatially localised states (Bergeon & Knobloch 2008*b*). More recent work focused on a full characterisation of these localised states and on the emergence of chaos in large-aspect-ratio domains (Beaume, Bergeon & Knobloch 2013*a*,*b*, 2018; Beaume 2020). Most of the pattern formation introduced in the above references can be found close to onset but they have, mostly, been studied for a certain set of parameter values. Despite the fact that a comprehensive linear stability analysis in the special case of balancing thermal and solutal gradients has been available for more than two decades (Ghorayeb & Mojtabi 1997), the analysis for unbalanced gradients was only recently attempted by Shankar, Kumar & Shivakumara (2021). Further, little is known about the dynamics near onset in the balanced case besides its linear regime, which makes it difficult to extrapolate the dynamics of the system away from the parameter values used in previous studies. Here, we perform a weakly nonlinear analysis and augment it by numerically continuing branches of spatially periodic states in a small-aspect-ratio domain. Our present work extends the previous analyses to a wider range of parameter values. In the next section, we present the mathematical framework associated with our case of doubly diffusive convection. In § 3, we detail the weakly nonlinear analysis of this system, followed by a characterisation of the nonlinear dynamics in § 4. We conclude in § 5 with a short discussion.

https://doi.org/10.1017/jfm.2021.1121 Published online by Cambridge University Press

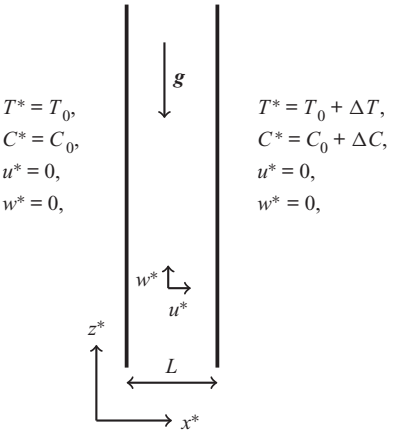


Figure 1. Sketch of the two-dimensional domain of interest together with the dimensional form of the boundary conditions.

2. Mathematical formulation

We consider the natural doubly diffusive convection of an incompressible fluid in a two-dimensional domain with periodic boundary conditions in the vertical direction. The sidewalls are rigid, impermeable and maintained at fixed temperatures and solutal concentration. The right wall is held at a higher temperature ($T_0 + \Delta T$) and solutal concentration ($C_0 + \Delta C$) than the left wall, where the temperature is T_0 and the solutal concentration is C_0. This configuration is depicted in figure 1.

The system is governed by the Navier–Stokes equation for fluid momentum, the incompressibility condition and advection–diffusion equations for both the temperature and the concentration. Cross-diffusion due to the Soret and Dufour effects is not considered. The imposed temperature and solutal concentration differences are assumed to be small enough so that the Boussinesq approximation can be applied, whereby density variations are neglected except in buoyancy terms. The density of the fluid is assumed to have a linear dependence on its temperature and concentration

$$\rho^* = \rho_0 + \rho_T(T^* - T_0) + \rho_C(C^* - C_0), \tag{2.1}$$

where ρ_0 is the density of the fluid at temperature T_0 and concentration C_0 and $\rho_T < 0$ (respectively $\rho_C > 0$) is the thermal (respectively solutal) expansion coefficient.

We introduce the non-dimensional quantities

$$\boldsymbol{x} = \frac{\boldsymbol{x}^*}{L}, \quad t = \frac{t^*}{L^2/\kappa}, \quad \boldsymbol{u} = \frac{\boldsymbol{u}^*}{\kappa/L}, \quad T = \frac{T^* - T_0}{\Delta T}, \quad C = \frac{C^* - C_0}{\Delta C}, \quad p = \frac{p^*}{\rho_0 \kappa \nu / L^2}, \tag{2.2a–f}$$

where L is the wall separation, κ is the rate of thermal diffusivity and ν is the kinematic viscosity. The non-dimensional governing equations for the fluid velocity $\boldsymbol{u} = u\hat{\boldsymbol{x}} + w\hat{\boldsymbol{z}}$, the pressure p, the temperature T and the concentration C thus read

$$\frac{1}{Pr}\left(\frac{\partial \boldsymbol{u}}{\partial t} + \boldsymbol{u}\cdot\boldsymbol{\nabla}\boldsymbol{u}\right) = -\boldsymbol{\nabla}p + \nabla^2\boldsymbol{u} + Ra\,(T + NC)\,\hat{\boldsymbol{z}}, \tag{2.3}$$

https://doi.org/10.1017/jfm.2021.1121 Published online by Cambridge University Press

$$\boldsymbol{\nabla}\cdot\boldsymbol{u}=0, \tag{2.4}$$

$$\frac{\partial T}{\partial t}+\boldsymbol{u}\cdot\boldsymbol{\nabla}T=\boldsymbol{\nabla}^2T, \tag{2.5}$$

$$\frac{\partial C}{\partial t}+\boldsymbol{u}\cdot\boldsymbol{\nabla}C=\frac{1}{Le}\nabla^2C, \tag{2.6}$$

where $\hat{\boldsymbol{z}}$ is the vertical ascending unit vector and where we have introduced the following dimensionless parameters:

$$\text{the Prandtl number } Pr=\frac{\nu}{\kappa}, \tag{2.7}$$

$$\text{the Rayleigh number } Ra=\frac{gL^3|\rho_T|\Delta T}{\rho_0\nu\kappa}, \tag{2.8}$$

$$\text{the buoyancy ratio } N=\frac{\rho_C\Delta C}{\rho_T\Delta T} \tag{2.9}$$

$$\text{and the Lewis number } Le=\frac{\kappa}{D}, \tag{2.10}$$

where D is the rate of solutal diffusivity. The non-dimensional boundary conditions read

$$u=0,\quad w=0,\quad -\frac{\partial p}{\partial x}+\frac{\partial^2u}{\partial x^2}=0,\quad T=0,\quad C=0\quad \text{on } x=0, \tag{2.11}$$

$$u=0,\quad w=0,\quad -\frac{\partial p}{\partial x}+\frac{\partial^2u}{\partial x^2}=0,\quad T=1,\quad C=1\quad \text{on } x=1, \tag{2.12}$$

where the pressure boundary condition is the projection of the Navier–Stokes equation on the boundary. Each variable is periodic in the vertical direction.

We restrict our attention to the case $N=-1$, where the full system (2.3)–(2.6), (2.11), (2.12) admits the steady conduction state with linear temperature and concentration profiles between the sidewalls

$$\boldsymbol{u}=\boldsymbol{0},\quad T=x,\quad C=x. \tag{2.13a–c}$$

We further introduce convective variables as the departures of the temperature and concentration from the conduction state

$$\Theta=T-x, \tag{2.14}$$

$$\Phi=C-x. \tag{2.15}$$

Using these new variables, the conduction state takes the form

$$\boldsymbol{u}=\boldsymbol{0},\quad \Theta=0,\quad \Phi=0, \tag{2.16a–c}$$

and system (2.3)–(2.6) can be written as

$$\frac{1}{Pr}\left(\frac{\partial\boldsymbol{u}}{\partial t}+\boldsymbol{u}\cdot\boldsymbol{\nabla}\boldsymbol{u}\right)=-\boldsymbol{\nabla}p+\nabla^2\boldsymbol{u}+Ra\,(\Theta-\Phi)\,\hat{\boldsymbol{z}}, \tag{2.17}$$

$$\boldsymbol{\nabla}\cdot\boldsymbol{u}=0, \tag{2.18}$$

$$\frac{\partial\Theta}{\partial t}+\boldsymbol{u}\cdot\boldsymbol{\nabla}\Theta=-u+\nabla^2\Theta, \tag{2.19}$$

$$\frac{\partial\Phi}{\partial t}+\boldsymbol{u}\cdot\boldsymbol{\nabla}\Phi=-u+\frac{1}{Le}\nabla^2\Phi. \tag{2.20}$$

https://doi.org/10.1017/jfm.2021.1121 Published online by Cambridge University Press

This formulation involving the convective variables allows the identification of two symmetries of the system: the reflection S_Δ and the continuous translation T_δ:

$$S_\Delta : \quad (x, z) \mapsto (1 - x, -z), \quad (u, w, \Theta, \Phi) \mapsto -(u, w, \Theta, \Phi), \tag{2.21}$$

$$T_\delta : \quad (x, z) \mapsto (x, z + \delta), \quad (u, w, \Theta, \Phi) \mapsto (u, w, \Theta, \Phi). \tag{2.22}$$

With periodic boundary conditions, these generate the symmetry group $O(2)$ and restrict the types of bifurcation that can occur from the conduction state.

3. Weakly nonlinear predictions

To predict the pattern formation present in our system, we start by performing the linear stability analysis of the conduction state $(u, w, p, \Theta, \Phi) = (0, 0, 0, 0, 0)$, which was previously done by Ghorayeb & Mojtabi (1997) and by Xin *et al.* (1998). We briefly rederive their results in the following subsection so that they can be applied in the later weakly nonlinear analysis, where we derive Ginzburg–Landau equations to model the small-amplitude behaviour close to the primary bifurcation for all Lewis and Prandtl numbers.

3.1. *Linear stability analysis*

We first consider small-amplitude stationary normal mode perturbations to the conduction state

$$(u, w, p, \Theta, \Phi)^{\mathrm{T}} = \epsilon((U_1(x), W_1(x), P_1(x), \Theta_1(x), \Phi_1(x))^{\mathrm{T}} \, \mathrm{e}^{\mathrm{i}kz} + \text{c.c.}) + O(\epsilon^2), \tag{3.1}$$

where c.c. denotes the complex conjugate of the preceding term, $\epsilon \ll 1$, and k is the vertical wavenumber and λ is the temporal growth rate of the perturbation. Inserting expansion (3.1) into system (2.17)–(2.20) and linearising the resulting system yields the eigenvalue problem

$$\mathcal{L}(Ra)\boldsymbol{\Psi_1} = \mathbf{0}, \tag{3.2}$$

for Ra and $\boldsymbol{\Psi}_1$ where

$$\boldsymbol{\Psi_1} = (U_1, W_1, P_1, \Theta_1, \Phi_1)^{\mathrm{T}} \, \mathrm{e}^{\mathrm{i}kz} + \text{c.c.}, \tag{3.3}$$

and

$$\mathcal{L}(Ra) = \begin{pmatrix} \nabla^2 & 0 & -\partial_x & 0 & 0 \\ 0 & \nabla^2 & -\partial_z & Ra & -Ra \\ \partial_x & \partial_z & 0 & 0 & 0 \\ -1 & 0 & 0 & \nabla^2 & 0 \\ -1 & 0 & 0 & 0 & \dfrac{1}{Le}\nabla^2 \end{pmatrix}. \tag{3.4}$$

The complex functions U_1, W_1, P_1, Θ_1 and Φ_1 satisfy Dirichlet boundary conditions on the sidewalls for the velocity, temperature and concentration perturbations

$$U_1(x) = W_1(x) = \Theta_1(x) = \Phi_1(x) = 0 \quad \text{on } x = 0, 1, \tag{3.5}$$

and the projection of the Navier–Stokes equation onto the boundary for the pressure perturbation

$$0 = -\frac{\partial P_1}{\partial x} + \frac{\partial^2 U_1}{\partial^2 x} \quad \text{on } x = 0, 1. \tag{3.6}$$

Solutions to (3.2)–(3.6) are independent of Pr and satisfy $\Phi_1 = Le\,\Theta_1$. Consequently, the only parameter dependence in the linear problem comes from the buoyancy term

https://doi.org/10.1017/jfm.2021.1121 Published online by Cambridge University Press

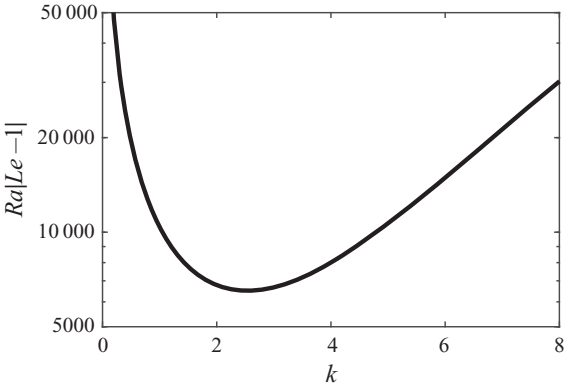


Figure 2. Marginal stability curve for the onset of doubly diffusive convection. The conduction state is stable to modes with wavenumber k below the curve, and unstable to them above. The minimum of this curve is $Ra_c|Le-1| \approx 6509$ with wavenumber $k_c \approx 2.5318$ and corresponds to the location of the primary bifurcation.

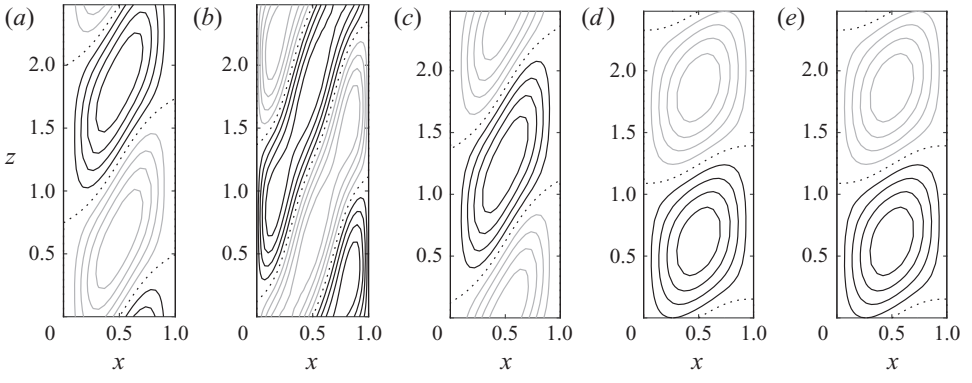


Figure 3. Contour plots of a single wavelength of the real critical eigenvector $\boldsymbol{\Psi}_1$ for $Le = 11$ ($k_c \approx 2.53$). The profiles show the perturbations in (*a*) horizontal velocity, u, (*b*) vertical velocity, w, (*c*) velocity streamfunction, ψ, where $u = -\psi_z$ and $w = \psi_x$, and in the convective variables (*d*) Θ and (*e*) Φ. Black (grey, dotted) lines indicate positive (negative, zero) values and are separated by 20 % of the maximum absolute value.

in the momentum equation, which takes the form $Ra(1-Le)\Theta_1$. The accordingly simplified version of (3.2) is then solved using a spectral eigenvalue solver based on a Chebyshev–Legendre collocation method for a range of k to determine the marginal stability curve in figure 2. This curve reveals a minimum at $k_c \approx 2.5318$ and $Ra_c|Le-1| \approx 6509$, which corresponds to the primary instability of the conduction state. The absolute value here comes from the fact that the system resulting from left wall heating and that resulting from right wall heating are equivalent. Contour plots presenting the fields for the velocity components, streamfunction and convective variables of this eigenmode for $Le = 11$ are shown in figure 3. The conduction state is thus first unstable to a spatially periodic state constituted of counter-rotating convection rolls that, when $Le > 1$, slant downwards from the hotter wall, filling the domain and extending to the cold wall.

The conduction state can also undergo Hopf bifurcations, where the growth rate is purely imaginary. However, for the parameter values tested, these bifurcations occurred for Rayleigh numbers that are orders of magnitude larger than that of the primary stationary bifurcation and are therefore out of the scope of the present work.

https://doi.org/10.1017/jfm.2021.1121 Published online by Cambridge University Press

3.2. *Weakly nonlinear analysis*

To investigate the weakly nonlinear regime around this primary bifurcation, we set $Ra = Ra_c + \epsilon^2 r$ with $r = O(1)$ and $\epsilon \ll 1$ and assume that the system evolves on a slow temporal scale $T_1 = \epsilon^2 t$. We also introduce a long spatial scale, $Z = \epsilon z$, to allow small-amplitude states with long spatial modulations. The small-aspect-ratio domains considered in the numerical computations in § 4 do not permit these long-scale modulations, so terms involving derivatives with respect to Z may be ignored in the subsequent analysis with no effect on the main result of this section: the criticality of the primary bifurcation. However, this long spatial variable has been included here to broaden the scope of the analysis and will be considered in future work. We emphasise that each of the state variables of our system (u, w, p, Θ and Φ) depend upon the independent variables: x, z, Z and T_1. Using this multiple-scale approach, the partial derivatives become

$$\frac{\partial}{\partial t} \mapsto \epsilon^2 \frac{\partial}{\partial T_1} \quad \text{and} \quad \frac{\partial}{\partial z} \mapsto \frac{\partial}{\partial z} + \epsilon \frac{\partial}{\partial Z}. \tag{3.7a,b}$$

Introducing the notation $\boldsymbol{\Psi} = (u, w, p, \Theta, \Phi)^{\mathrm{T}}$, we can express each of the variables as a perturbation expansion in ϵ about the conduction state $\boldsymbol{\Psi}_0 = (0, 0, 0, 0, 0)^{\mathrm{T}}$

$$\boldsymbol{\Psi} = \boldsymbol{\Psi}_0 + \epsilon \boldsymbol{\Psi}_1 + \epsilon^2 \boldsymbol{\Psi}_2 + \ldots, \tag{3.8}$$

where $\boldsymbol{\Psi}_j = (u_j, w_j, p_j, \theta_j, \phi_j)^{\mathrm{T}}$ is the correction at $O(\epsilon^j)$ for $j = 1, 2, \ldots$.

The corrections are periodic in z and also satisfy homogeneous boundary conditions at each order in ϵ

$$u_j = w_j = \theta_j = \phi_j = 0 \quad \text{on } x = 0, 1, \quad j = 1, 2, \ldots, \tag{3.9}$$

as well as the pressure boundary condition

$$\frac{\partial^2 u_j}{\partial x^2} - \frac{\partial p_j}{\partial x} = 0 \quad \text{on } x = 0, 1, \quad j = 1, 2, \ldots. \tag{3.10}$$

The expansion (3.8) is substituted into the full system (2.17)–(2.20) and the perturbations are solved numerically order by order in ϵ using an extension of the aforementioned collocation method. By further extracting the parameter dependence of the perturbations at each order, we obtain a Ginzburg–Landau equation that can be applied for all parameter values and will indicate the criticality of the primary bifurcation.

We proceed by detailing this formulation, which should be applied to the cases $Le > 1$ and $Le < 1$ separately, owing to the parameter combination $Ra(1 - Le)$ changing sign between them. However, the results for $Le < 1$ can be related to those for $Le > 1$ by using an alternative non-dimensionalisation to (2.2*a–f*) involving the solutal diffusivity, D, instead of thermal diffusivity, κ, which results in a set of equations like (2.3)–(2.6), except with T and C exchanged and the Lewis, Prandtl and Rayleigh numbers replaced by the inverse Lewis number, Schmidt number, $Sc = LePr$, and solutal Rayleigh number, $Ra_S = -RaNLe$, respectively.

The conduction state solves the system at leading order. At $O(\epsilon)$, the correction is given by the solution to linear system (3.2)

$$\boldsymbol{\Psi}_1 = A_1(Z, T_1)\,(U_1(x), W_1(x), P_1(x), \Theta_1(x), Le\Theta_1(x))^{\mathrm{T}}\, \mathrm{e}^{\mathrm{i}k_c z} + \text{c.c.}, \tag{3.11}$$

where k_c is the critical wavenumber. No phase constraint is applied at this point, but the amplitude of the eigenfunction is fixed using

$$\langle U_1, U_1 \rangle + \langle W_1, W_1 \rangle + \langle P_1, P_1 \rangle + \langle \Theta_1, \Theta_1 \rangle = 1, \tag{3.12}$$

https://doi.org/10.1017/jfm.2021.1121 Published online by Cambridge University Press

f_{ij}		j		
		0	1	2
	1	$\bar{U}_1 \frac{\mathrm{d}U_1}{\mathrm{d}x} + \mathrm{i}k_c \bar{W}_1 U_1 + \mathrm{c.c.}$	$-2\mathrm{i}k_c U_1$	$U_1 \frac{\mathrm{d}U_1}{\mathrm{d}x} + \mathrm{i}k_c W_1 U_1$
	2	$\bar{U}_1 \frac{\mathrm{d}W_1}{\mathrm{d}x} + \mathrm{i}k_c \bar{W}_1 W_1 + \mathrm{c.c.}$	$-2\mathrm{i}k_c W_1 + P_1$	$U_1 \frac{\mathrm{d}W_1}{\mathrm{d}x} + \mathrm{i}k_c W_1^2$
i	3	0	$-W_1$	0
	4	$\bar{U}_1 \frac{\mathrm{d}\Theta_1}{\mathrm{d}x} + \mathrm{i}k_c \bar{W}_1 \Theta_1 + \mathrm{c.c.}$	$-2\mathrm{i}k_c \Theta_1$	$U_1 \frac{\mathrm{d}\Theta_1}{\mathrm{d}x} + \mathrm{i}k_c W_1 \Theta_1$

Table 1. Functions f_{ij} ($i = 1, 2, 3, 4, j = 0, 1, 2$) in the nonlinear term $\mathcal{N}_2$ at $O(\epsilon^2)$ in (3.14). The overbar denotes complex conjugation.

with the inner product

$$\langle f, g \rangle = \frac{1}{\lambda_c} \int_0^{\lambda_c} \int_0^1 \bar{f}^{\mathrm{T}} g \, \mathrm{d}x \, \mathrm{d}z, \tag{3.13}$$

where $\lambda_c = 2\pi/k_c$ is the wavelength of the critical eigenvector, the overbar denotes complex conjugation and the superscript T denotes the transposition operation when f is a vector. Due to the lack of available explicit expressions for the solutions to this perturbation problem, these inner products need to be computed numerically, which we achieved by using the Clenshaw–Curtis quadrature on the collocation nodes used in § 3.1. The amplitude A_1 evolves over both long spatial and temporal scales according to an amplitude equation that will be determined at higher order.

At $O(\epsilon^2)$, the linear operator $\mathcal{L}$ acts on the second-order terms and is forced by both the nonlinear terms between the $O(\epsilon)$ corrections and terms proportional to the slow spatial derivative of the $O(\epsilon)$ correction A_{1Z}

$$\mathcal{L}(Ra_c)\boldsymbol{\Psi}_2 = \underbrace{\begin{pmatrix} \frac{1}{Pr} f_{10} |A_1|^2 + \left(A_{1Z} f_{11} \mathrm{e}^{\mathrm{i}k_c z} + \mathrm{c.c.}\right) + \frac{1}{Pr}\left(f_{12} A_1^2 \mathrm{e}^{2\mathrm{i}k_c z} + \mathrm{c.c.}\right) \\ \frac{1}{Pr} f_{20} |A_1|^2 + \left(A_{1Z} f_{21} \mathrm{e}^{\mathrm{i}k_c z} + \mathrm{c.c.}\right) + \frac{1}{Pr}\left(f_{22} A_1^2 \mathrm{e}^{2\mathrm{i}k_c z} + \mathrm{c.c.}\right) \\ \left(A_{1Z} f_{31} \mathrm{e}^{\mathrm{i}k_c z} + \mathrm{c.c.}\right) \\ f_{40} |A_1|^2 + \left(A_{1Z} f_{41} \mathrm{e}^{\mathrm{i}k_c z} + \mathrm{c.c.}\right) + \left(f_{42} A_1^2 \mathrm{e}^{2\mathrm{i}k_c z} + \mathrm{c.c.}\right) \\ Le f_{40} |A_1|^2 + \left(A_{1Z} f_{41} \mathrm{e}^{\mathrm{i}k_c z} + \mathrm{c.c.}\right) + Le\left(f_{42} A_1^2 \mathrm{e}^{2\mathrm{i}k_c z} + \mathrm{c.c.}\right) \end{pmatrix}}_{\mathcal{N}_2}, \tag{3.14}$$

where the functions $f_{ij}(x)$ for $i = 1, 2, 3, 4$ and $j = 0, 1, 2$ are independent of Pr and Le and are given in table 1.

To ensure the existence of a unique solution at this order, we derive a solvability condition using the Fredholm alternative theorem. This involves the adjoint operator to $\mathcal{L}$, $\mathcal{L}^\dagger$, defined through the relationship

$$\langle f, \mathcal{L} g \rangle = \langle \mathcal{L}^\dagger f, g \rangle, \tag{3.15}$$

https://doi.org/10.1017/jfm.2021.1121 Published online by Cambridge University Press

which holds for all vector functions f and g. Integrating the left-hand side by parts, we find that the adjoint operator takes the form

$$\mathcal{L}^\dagger = \begin{pmatrix} \nabla^2 & 0 & -\partial_x & -1 & -1 \\ 0 & \nabla^2 & -\partial_z & 0 & 0 \\ \partial_x & \partial_z & 0 & 0 & 0 \\ 0 & Ra_c & 0 & \nabla^2 & 0 \\ 0 & -Ra_c & 0 & 0 & \dfrac{1}{Le}\nabla^2 \end{pmatrix}, \tag{3.16}$$

together with the adjoint boundary conditions

$$u^\dagger = 0, \quad w^\dagger = 0, \quad \theta^\dagger = 0, \quad \phi^\dagger = 0 \quad \text{on } x = 0, 1, \tag{3.17}$$

$$\frac{\partial^2 u^\dagger}{\partial x^2} - \frac{\partial p^\dagger}{\partial x} = 0 \quad \text{on } x = 0, 1, \tag{3.18}$$

and periodicity in the vertical direction.

The Fredholm alternative allows us to pose the adjoint problem

$$\mathcal{L}^\dagger \boldsymbol{\Psi}^\dagger = \mathbf{0}, \tag{3.19}$$

whose solution is unique up to a vertical translation and a multiplicative constant. This solution may be written in the form

$$\boldsymbol{\Psi}^\dagger = \left(U^\dagger(x), W^\dagger(x), P^\dagger(x), \frac{1}{1-Le}\Theta^\dagger(x), -\frac{Le}{1-Le}\Theta^\dagger(x) \right)^{\mathrm{T}} \mathrm{e}^{\mathrm{i}k_c z} + \text{c.c.}, \tag{3.20}$$

where the parameter dependence of the components has been extracted. The amplitude and phase are fixed by imposing the conditions

$$\langle U^\dagger, U^\dagger \rangle + \langle W^\dagger, W^\dagger \rangle + \langle P^\dagger, P^\dagger \rangle + \langle \Theta^\dagger, \Theta^\dagger \rangle = 1, \tag{3.21}$$

and

$$\mathrm{Im}(\langle U^\dagger, U_1 \rangle) = 0, \tag{3.22}$$

where Im represents the imaginary part, respectively.

Using this adjoint solution, we then apply the $O(\epsilon^2)$ solvability condition

$$\langle \Psi^\dagger, \mathcal{N}_2 \rangle = 0. \tag{3.23}$$

Owing to the vertical wavenumber dependence of terms in $\mathcal{N}_2$, the only non-trivial contributions come from those proportional to A_{1Z} and their complex conjugates and (3.23) then reduces to

$$-2\mathrm{i}k_c\langle U^\dagger, U_1 \rangle - 2\mathrm{i}k_c\langle W^\dagger, W_1 \rangle + \langle W^\dagger, P_1 \rangle - \langle P^\dagger, W_1 \rangle - 2\mathrm{i}k_c\langle \Theta^\dagger, \Theta_1 \rangle = 0, \tag{3.24}$$

which may be further simplified to

$$\left\langle \boldsymbol{\Psi}^\dagger, \frac{\partial \mathcal{L}\boldsymbol{\Psi}_1}{\partial k_c} \right\rangle = 0. \tag{3.25}$$

Thus, this solvability condition is automatically satisfied as the primary bifurcation occurs at a quadratic minimum of the marginal stability curve (see figure 2).

https://doi.org/10.1017/jfm.2021.1121 Published online by Cambridge University Press

The $O(\epsilon^2)$ system (3.14) can be solved to find that the second-order correction to the conduction state is

$$\boldsymbol{\Psi}_2 = |A_1|^2\boldsymbol{\Psi}_2^0 + ((A_2\boldsymbol{\Psi}_1 + A_{1Z}\boldsymbol{\Psi}_2^1)\mathrm{e}^{\mathrm{i}k_c z} + \text{c.c.}) + (A_1^2\boldsymbol{\Psi}_2^2\mathrm{e}^{2\mathrm{i}k_c z} + \text{c.c.}), \tag{3.26}$$

where $\boldsymbol{\Psi}_2 = (u_2, w_2, p_2, \theta_2, \phi_2)^{\mathrm{T}}$ and the functions $\boldsymbol{\Psi}_2^i$ for $i = 0, 1, 2$ have the following parameter dependence:

$$\boldsymbol{\Psi}_2^0 = \left(0, \frac{1}{Pr}\tilde{w}_2 + (1+Le)\tilde{w}_3, \frac{1}{Pr}\tilde{p}_2, \tilde{\theta}_3, Le^2\tilde{\theta}_3\right)^{\mathrm{T}}, \tag{3.27}$$

$$\boldsymbol{\Psi}_2^1 = \left(\tilde{u}_7, \tilde{w}_7, \tilde{p}_7, \tilde{\theta}_7, Le\,\tilde{\theta}_7\right)^{\mathrm{T}}, \tag{3.28}$$

$$\begin{aligned}\boldsymbol{\Psi}_2^2 = \Bigg(&\frac{1}{Pr}\left(\tilde{u}_4, \tilde{w}_4, \tilde{p}_4, \tilde{\theta}_4, Le\tilde{\theta}_4\right) + (1+Le)(\tilde{u}_5, \tilde{w}_5, \tilde{p}_5, 0, 0)\\ &+ (0,0,0,\tilde{\theta}_5, Le^2\tilde{\theta}_5) + Le(0,0,0,\tilde{\theta}_6,\tilde{\theta}_6)\Bigg)^{\mathrm{T}}.\end{aligned} \tag{3.29}$$

The newly introduced functions $\tilde{u}_i$, $\tilde{w}_i$, $\tilde{p}_i$ and $\tilde{\theta}_i$ for $i = 2, \ldots, 7$ are independent of Le and Pr and satisfy (A1)–(A5) in § A.1 of the Appendix A.

Continuing to $O(\epsilon^3)$, both the deviation away from the critical Rayleigh number and the slow time dependence of the solution appear in the right-hand side of the resulting system, in addition to nonlinear terms between first and second-order corrections and terms with slow spatial derivatives. The system to solve at third order is

$$\mathcal{L}(Ra_c)\boldsymbol{\Psi}_3 = \underbrace{\begin{pmatrix} \frac{1}{Pr}\left(\frac{\partial u_1}{\partial_{T_1}} + J(\boldsymbol{u}, u)\right) - 2\frac{\partial^2 u_2}{\partial z \partial Z} - \frac{\partial^2 u_1}{\partial Z^2} \\ \frac{1}{Pr}\left(\frac{\partial w_1}{\partial_{T_1}} + J(\boldsymbol{u}, w)\right) - r\,(\theta_1 - \phi_1) - 2\frac{\partial^2 w_2}{\partial z \partial Z} - \frac{\partial^2 w_1}{\partial Z^2} + \frac{\partial p_2}{\partial Z} \\ -\frac{\partial w_2}{\partial Z} \\ \left(\frac{\partial \theta_1}{\partial_{T_1}} + J(\boldsymbol{u}, \theta)\right) - 2\frac{\partial^2 \theta_2}{\partial z \partial Z} - \frac{\partial^2 \theta_1}{\partial Z^2} \\ \left(\frac{\partial \phi_1}{\partial_{T_1}} + J(\boldsymbol{u}, \phi)\right) - \frac{2}{Le}\frac{\partial^2 \phi_2}{\partial z \partial Z} - \frac{1}{Le}\frac{\partial^2 \phi_1}{\partial Z^2} \end{pmatrix}}_{\mathcal{N}_3}, \tag{3.30}$$

where the advective terms are

$$J(\boldsymbol{u}, f) = \boldsymbol{u}_1 \cdot \boldsymbol{\nabla} f_2 + \boldsymbol{u}_2 \cdot \boldsymbol{\nabla} f_1 + w_1 \partial_Z f_1, \tag{3.31}$$

where f_1 and f_2, respectively, refer to the first- and second-order corrections of the variables $f = u, w, \theta$ and ϕ.

The solvability condition at this order

$$\langle \boldsymbol{\Psi}^\dagger, \mathcal{N}_3 \rangle = 0, \tag{3.32}$$

is no longer trivially satisfied because some nonlinear terms contained in $\mathcal{N}_3$ have $e^{ik_c z}$ dependence arising from terms proportional to A_1, $|A_1|^2 A_1$, A_{1ZZ}, A_{2Z} and their

https://doi.org/10.1017/jfm.2021.1121 Published online by Cambridge University Press

	Term in the Ginzburg–Landau equation (3.33)			
	αA_{1T_1}	$\gamma r A_1$	$\beta\lvert A_1\rvert^2 A_1$	δA_{1ZZ}
Terms in $\mathcal{N}_3$ proportional to	$\dfrac{\partial f_1}{\partial T_1}$	$r(\theta_1 - \phi_1)$	$\boldsymbol{u}_1 \cdot \nabla f_2$	$\dfrac{\partial^2 f_2}{\partial z \partial Z}, \dfrac{\partial^2 f_1}{\partial Z^2}$
			$\boldsymbol{u}_2 \cdot \nabla f_1$	$\dfrac{\partial p_2}{\partial Z}, \dfrac{\partial w_2}{\partial Z}$

Table 2. Terms from $\mathcal{N}_3$ (see (3.30)) contributing to the Ginzburg–Landau equation (3.33). The column in which these terms are placed informs on the term to which they contribute. Here, f_1 and f_2, respectively refer to first- and second-order corrections of the variables $f = u, w, \theta$ and ϕ.

complex conjugates. However, the contributions to (3.32) from terms proportional to A_{2Z}, cancel for the same reason that the solvability condition at $O(\epsilon^2)$ was satisfied. Consequently, A_2 remains arbitrary at this order. Collecting the remaining terms from (3.32), we obtain the Ginzburg–Landau equation, that holds for both $Le > 1$ and $Le < 1$

$$\alpha A_{1T_1} = \gamma r A_1 + \beta |A_1|^2 A_1 + \delta A_{1ZZ}, \tag{3.33}$$

where table 2 indicates which terms of $\mathcal{N}_3$ contribute to each term above. This equation is equivariant under the $O(2)$ symmetry so we may choose the phase of the $O(\epsilon)$ correction so that these coefficients are real. The coefficient δ is independent of the physical parameters Pr and Le, while α, β and γ satisfy the relations

$$\alpha = \frac{1}{Pr}\alpha_1 + (1 + Le)\alpha_2, \tag{3.34}$$

$$\beta = \frac{1}{Pr^2}\beta_1 + \frac{1 + Le}{Pr}\beta_2 + (1 + Le^2)\beta_3 + Le\,\beta_4, \tag{3.35}$$

$$\gamma = (1 - Le)\gamma_1, \tag{3.36}$$

where full expressions used to obtain α_i, β_i, γ_1 and δ are provided in (A6)–(A9) and evaluated in table 4 in § A.2. By dividing (3.33) through by α, (3.33) is more conveniently written as

$$A_{1T_1} = a_1 r A_1 + a_2 |A_1|^2 A_1 + a_3 A_{1ZZ}, \tag{3.37}$$

where $a_1 = \gamma/\alpha$, $a_2 = \beta/\alpha$ and $a_3 = \delta/\alpha$.

The solutions to the Ginzburg–Landau equation (3.37) are good approximations of the small-amplitude solutions of the full doubly diffusive system (2.17)–(2.20). Of particular interest here are the two steady solutions that are invariant with respect to the long spatial scale Z. The first of these solutions is the trivial solution

$$A_1 = 0. \tag{3.38}$$

This solution is valid for all r and corresponds to the conduction state (2.16*a–c*). The second important solution is

$$A_1 = \left(-\frac{a_1 r}{a_2}\right)^{1/2} \mathrm{e}^{\mathrm{i}\chi}, \tag{3.39}$$

https://doi.org/10.1017/jfm.2021.1121 Published online by Cambridge University Press

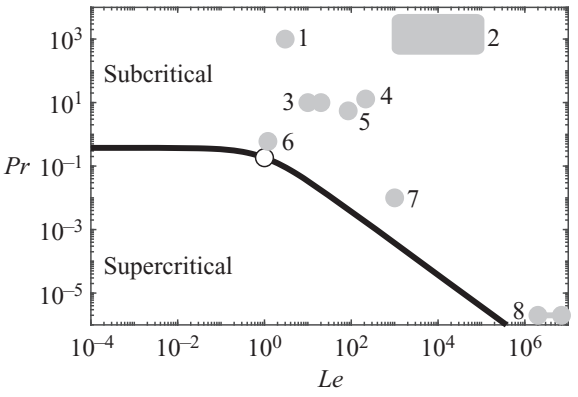


Figure 4. Boundary $a_2 = 0$ in (Le, Pr) parameter space separating the region where the primary bifurcation from the conduction state is subcritical (above) from that where it is supercritical (below). The conduction state is linearly stable for all Ra at $Le = 1$ and this point is indicated by the open circle. The grey regions indicate parameter values from Schmitt (1983) for the physical doubly diffusive systems: (1) salt/sugar, (2) magmas, (3) oxide semiconductors, (4) heat/salt 0 °C, (5) heat/salt 30 °C, (6) humidity/heat, (7) liquid metals and (8) stellar interiors.

where χ is an arbitrary phase. This solution relates to states of small-amplitude spatially periodic convection that can be found near the primary bifurcation. These fluid states can then be approximated by

$$(u, w, p, \Theta, \Phi)^{\mathrm{T}} \approx \sqrt{-\frac{a_1(Ra - Ra_c)}{a_2}}\,(U_1(x), W_1(x), P_1(x), \Theta_1(x), Le\Theta_1(x))^{\mathrm{T}}\,\mathrm{e}^{\mathrm{i}k_c z} + \text{c.c.}, \quad (3.40)$$

where the phase χ has been absorbed into z via a vertical translation. These states only exist at small amplitude for Rayleigh numbers that satisfy

$$\frac{a_1}{a_2}(Ra_c - Ra) > 0. \quad (3.41)$$

Consequently, the sign of the ratio a_1/a_2 determines the criticality of the primary bifurcation and the initial direction of branching.

Using the numerical values in table 4, we computed a_i over a range of parameter values. The coefficients a_1 and a_3 are positive for all Pr provided $Le \neq 1$, whereas the sign of a_2 changes as these parameters are varied. As a result, there exists a boundary in parameter space that separates regions where the primary bifurcation is subcritical ($a_2 > 0$) from those where it is supercritical ($a_2 < 0$). This boundary is shown in figure 4 and implies that, for any value of the Lewis number, there exists a critical value of the Prandtl number, $Pr_c(Le)$, expressed in terms of the physical parameters in (A15), above which the bifurcation is subcritical. This critical value tends to 0.376 for small Lewis numbers while it approaches the asymptotic relation $Pr_c \sim 0.376/Le$ as the Lewis number tends to infinity. We further note that the parameter values for physical doubly diffusive systems from Schmitt (1983) all lie within the region where the primary bifurcation is subcritical. While we are unaware of further fluid systems lying within the supercritical region of parameter space, we expect that they exist since some of the physical systems identified in figure 4, including humidity/heat and stellar interiors (marked (6) and (8), respectively), have parameter values that are within an order of magnitude of the sub/supercritical boundary.

https://doi.org/10.1017/jfm.2021.1121 Published online by Cambridge University Press

We can gain physical insight into the criticality of the primary bifurcation by examining the contributions that each of the nonlinear terms from (2.3)–(2.6) make to a_2, using a similar approach to the one Requilé *et al.* (2020) applied to plane Poiseuille and plane Couette flows with viscous dissipation. The expression of the coefficient β (3.35) and the corresponding numerical values provided in table 4 in the Appendix A, show that the inertial term $\boldsymbol{u}\cdot\boldsymbol{\nabla}\boldsymbol{u}$ (contributing to β_1 and β_2) provides a negative contribution to a_2, whereas thermal $\boldsymbol{u}\cdot\boldsymbol{\nabla}T$ and solutal $\boldsymbol{u}\cdot\boldsymbol{\nabla}C$ advective terms (mostly contributing to β_3 and β_4) provide a positive contribution to a_2. The latter statement is further justified in § A.3 in the Appendix A. It is therefore solutal and thermal advection in the system that drives the subcriticality of the primary bifurcation, while inertial effects drive the supercriticality. Thus, reducing the Prandtl number reduces the subcriticality of the bifurcation since the effects of inertia are strengthened.

The final term in the Ginzburg–Landau equation (3.37), a_3A_{1ZZ}, allows small-amplitude solutions of the doubly diffusive system to exhibit long-scale amplitude modulation. These solutions include phase-winding states that describe patterns whose wavenumbers are close to the critical wavenumber k_c (Cross *et al.* 1983), and spatially modulated states that can develop into localised states away from the primary bifurcation (Bergeon & Knobloch 2008*a*). These are out of the scope of the present work, but we will consider the effect of the term a_3A_{1ZZ} on spatially localised states in future work.

4. Fully nonlinear behaviour

Having established the region of (Le, Pr) parameter space in which the bifurcation is subcritical, we can now investigate the nonlinear behaviour of the system near the onset of convection. In particular, we focus on the structure and stability of the primary branch of spatially periodic convection states with wavenumber k_c as it extends towards larger amplitudes. For this, we consider a single-wavelength domain with $L_z = \lambda_c = 2\pi/k_c$, which precludes modulational instabilities arising in large domains that are captured by our weakly nonlinear analysis through the A_{1ZZ} term in (3.37).

We numerically continue the primary branch against the Rayleigh number across a range of Lewis ($Le \in [5, 100]$) and Prandtl ($Pr \in [2\times10^{-3}, 10]$) numbers. Cases for which $Le < 1$ can be extrapolated from our results by a suitable transformation. The solution branches will be identified on bifurcation diagrams showing either the total kinetic energy of steady states

$$E = \frac{1}{2}\int_0^{\lambda_c}\int_0^1 (u^2+w^2)\,\mathrm{d}x\,\mathrm{d}z, \tag{4.1}$$

or the average velocity $\|\boldsymbol{u}\|_2 = \sqrt{2E/\lambda_c}$, against the Rayleigh number Ra.

Computations were carried out using a spectral element numerical method based on a Gauss–Lobatto–Legendre discretisation (Bergeon & Knobloch 2002) and supplemented by Stokes preconditioning with $\Delta t = 0.1$, as detailed by Beaume (2017). Numerical results were validated against a discretisation of up to 4 spectral elements with 29 nodes in both the x and z directions. The stability of the steady states was computed using an Arnoldi method based on a time-stepping scheme (Mamun & Tuckerman 1995). Further direct numerical simulations used a stiffly stable second-order splitting scheme based on Karniadakis, Israeli & Orszag (1991) with time step $\Delta t = 10^{-3}$.

4.1. *Bifurcation structure*

The results can be summarised by dividing parameter space according to the qualitative nature of the bifurcation diagram. Figure 5(*a*) indicates the four main regimes found.

https://doi.org/10.1017/jfm.2021.1121 Published online by Cambridge University Press

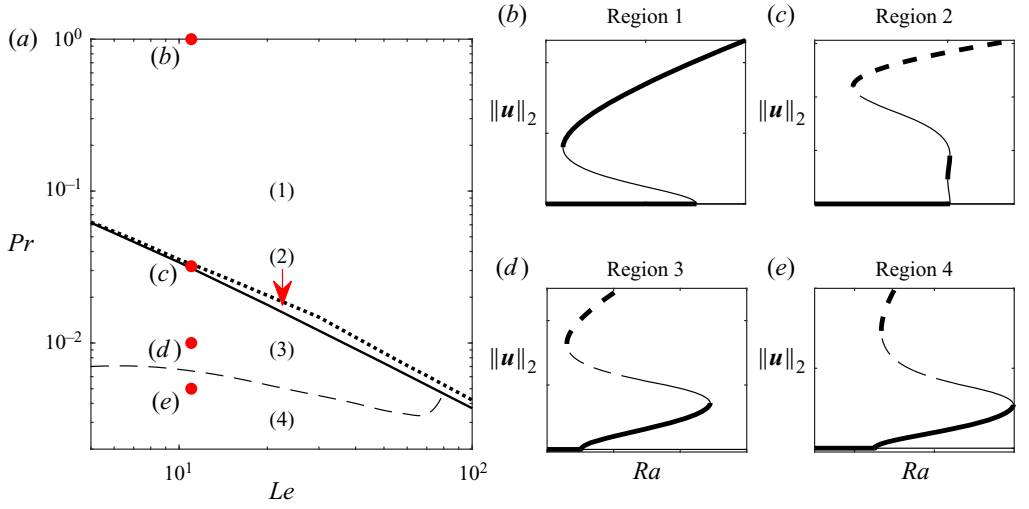


Figure 5. (*a*) Enlargement of a subset of the parameter space shown in figure 4 showing four regions where the bifurcation diagrams exhibit qualitatively different behaviours. The thick line separates subcritical from supercritical branching, while the additional region boundaries are identified with either dotted or dashed lines. (*b–e*) Representative bifurcation diagrams for parameter values within each of the four regions. The stability of the branch segments is also indicated using thick lines for stable solutions, thin lines for solutions unstable to amplitude perturbations and dashed lines for solutions unstable to drift. The location of bifurcations depend upon the specific parameter values used, so those used for each sketch have been marked in panel (*a*).

Region (1) describes the moderate and large Pr behaviour for all Le. In this region, the primary bifurcation is strongly subcritical and the primary branch has a single saddle node, as shown in figure 5(*b*). Parameter values within this region have received the most attention in previous studies focusing on subcritical pattern formation (e.g. see Xin *et al.* 1998; Bergeon & Knobloch 2008*b*). Region (2) occupies a small region of parameter space above the boundary $Pr = Pr_c$, where the primary bifurcation is weakly subcritical, and separates the typical subcritical behaviour in region (1) from the supercritical behaviour in regions (3) or (4). The steady convection state branches typically have three saddle nodes in region (2), as exemplified in figure 5(*c*). Regions (3) and (4) identify the two qualitatively different types of bifurcation diagrams observable when the primary bifurcation is supercritical. In both cases, the primary branch has two saddle nodes, with the first lying in the supercritical region $Ra > Ra_c$. The difference between the regions is the location of the second saddle node: in region (3), it is found for $Ra < Ra_c$ (see figure 5*d*), whereas, in region (4), it is found in $Ra > Ra_c$ (see figure 5*e*). Consequently, a large-amplitude convection state may coexist with the stable conduction state when the primary bifurcation is supercritical, but, for sufficiently small Pr, steady convection states are found entirely within the supercritical region, where the conduction state is unstable. There may exist a fifth region, where the primary branch increases monotonically in both Rayleigh number and in amplitude, but we have not identified it in this study.

We now determine the structure of the primary branch as Pr decreases for a fixed value of Le. To achieve this, we follow the locations of its three saddle nodes with respect to Ra and Pr. In doing so, we observed two different scenarios according to whether the pair of saddle nodes are created on the lower or upper part of the primary branch. These are exemplified in figure 6 for $Le = 11$ (representative of $5 \leqslant Le \lesssim 15$) and $Le = 20$ (representative of $19 \lesssim Le < 100$). Since the transition between the two scenarios

https://doi.org/10.1017/jfm.2021.1121 Published online by Cambridge University Press

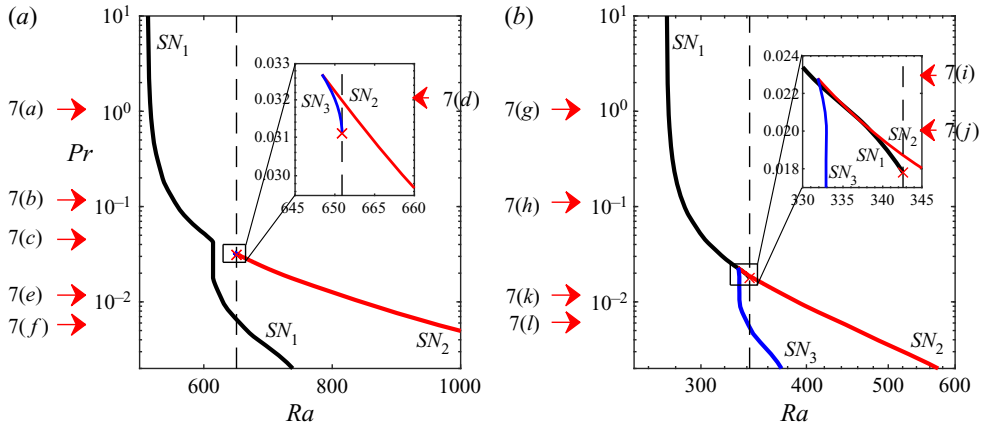


Figure 6. Location of the three saddle-node bifurcations of the primary branch in (Ra, Pr) parameter space for (a) $Le = 11$ and (b) $Le = 20$. The dashed line marks the critical Rayleigh number at which the primary bifurcation is found, Ra_c, and the cross marks the codimension two point (Ra_c, Pr_c) explained in the text. The insets provide enlargements of the area around Ra_c in each case. Arrows mark the bifurcation diagrams shown in figure 7.

occupies a small region of parameter space within region (2) for $15 \lesssim Le \lesssim 19$, we did not investigate it any further.

To help interpret the plots in figure 6, figure 7 demonstrates the evolution of the bifurcation diagrams as Pr decreases for $Le = 11$ $(a–f)$ and $Le = 20$ $(g–l)$. The structure of the bifurcation diagrams in region (1), for high Pr, remain similar, as shown in figures 7(a) and 7(g). From the primary bifurcation, the primary branch extends towards lower Rayleigh numbers and proceeds to turn around at a saddle node, hereafter referred to as SN_1, before heading towards large amplitude convection states at large Ra. Figure 6 suggests that, as $Pr \to \infty$, the location of SN_1 tends to a constant Rayleigh number, dependent upon Le. This figure also shows that SN_1 occurs at larger Ra as the Prandtl number is decreased and the primary bifurcation becomes less subcritical.

Upon decreasing the Prandtl number, the primary branch undergoes a cusp bifurcation at $Pr \approx Pr_{cusp}(Le) > Pr_c(Le)$, while still subcritical, denoting the beginning of region (2). The cusp produces two additional saddle nodes along the primary branch: SN_2 and SN_3. The exact process by which this is achieved depends on the Lewis number. For $Le \lesssim 15$, the cusp bifurcation occurs at smaller amplitude than SN_1 and the saddle nodes are labelled SN_3, SN_2, SN_1 as the branch is followed in the direction of increasing energy (see, for e.g. figure 7(d) for $Le = 11$ and $Pr = 0.032$, near the cusp parameter value: $Pr_{cusp} \approx 0.033$). In contrast, for $Le \gtrsim 19$, the cusp bifurcation occurs at higher amplitude than SN_1 and saddle nodes are labelled SN_1, SN_2, SN_3, as shown in figure 7(i) for $Le = 20$, $Pr = 0.023 \approx Pr_{cusp}$.

Continuing to reduce Pr across region (2) (from Pr_{cusp} to Pr_c), the Rayleigh number associated with SN_2 increases so that it reaches the supercritical region before $Pr = Pr_c$. During this transition, the saddle node with smallest amplitude (SN_3 for $Le \lesssim 15$; SN_1 for $Le \gtrsim 19$) moves to larger Rayleigh numbers but with decreasing amplitude until it collides with the primary bifurcation at $Pr = Pr_c$ and $Ra = Ra_c$, where the primary bifurcation changes from subcritical to supercritical. This process is highlighted in the insets of figure 6 and results in the primary branch possessing only two saddle nodes in the supercritical regime ($Pr < Pr_c$).

https://doi.org/10.1017/jfm.2021.1121 Published online by Cambridge University Press

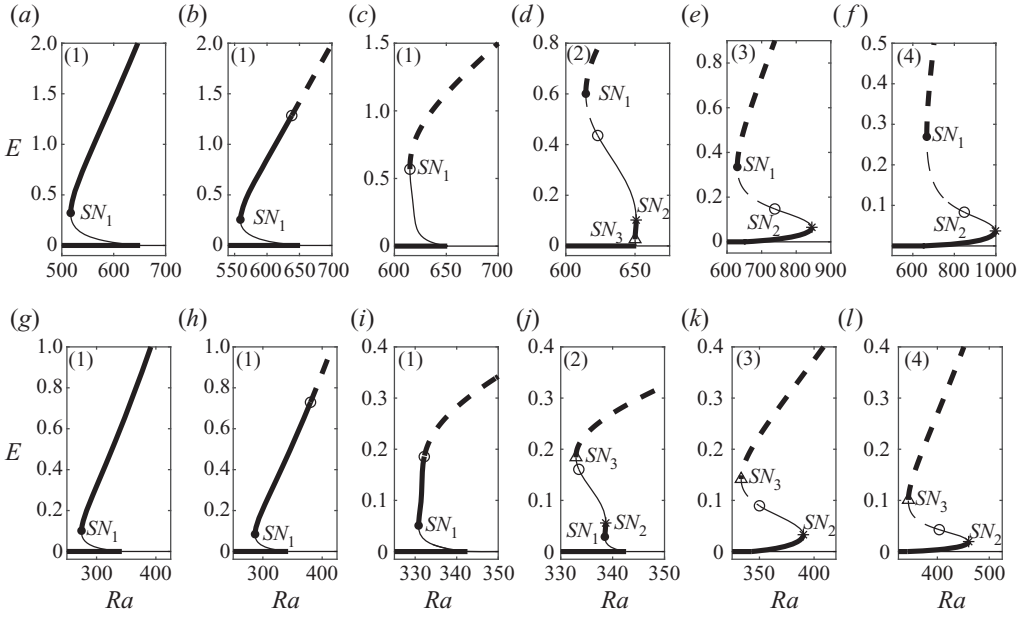


Figure 7. Bifurcation diagrams showing the primary branch of steady convection and the stability of the related states across the four regions, indicated in the top left corner. Thick lines indicate stable solutions, thin lines indicate solutions unstable to amplitude perturbations and dashed lines indicate solutions unstable to drift. Saddle nodes are marked by symbols: SN_1 (filled circle), SN_2 (asterisk) and SN_3 (triangle). The open circle corresponds to the destabilising drift bifurcation. The parameter values, also indicated by the arrows in figure 6, are: $Le = 11$, and (*a*) $Pr = 1$, (*b*) $Pr = 0.1$, (*c*) $Pr = 0.042$, (*d*) $Pr = 0.032$, (*e*) $Pr = 0.01$, (*f*) $Pr = 0.005$; as well as $Le = 20$, and (*g*) $Pr = 1$, (*h*) $Pr = 0.1$, (*i*) $Pr = 0.023$, (*j*) $Pr = 0.02$, (*k*) $Pr = 0.01$ and (*l*) $Pr = 0.005$. For $Le = 11$ (respectively $Le = 20$), $Pr_c \approx 0.031$, $Pr_{cusp} \approx 0.033$ (respectively $Pr_c \approx 0.018$, $Pr_{cusp} \approx 0.023$).

The locations of the remaining two saddle nodes go toward larger Ra as Pr decreases and are found in the supercritical region ($Ra > Ra_c$) in region (4), as shown in figure 5. It is therefore clear that multiple steady convection states can exist for the same parameter values near the onset of convection, regardless of the criticality of the primary bifurcation. This result extends earlier observations on the number of saddle-node bifurcations occurring along the primary branch in related systems (Tsitverblit & Kit 1993).

More insight into these results can be obtained by representing, as in figure 8, the location of the saddle nodes for various Lewis numbers as a function of the reduced Prandtl number Pr/Pr_c and combined parameter $Ra|Le - 1|$. These reduced parameters allow us to identify the location where the criticality of the primary bifurcation changes as the single coordinate point: $Pr/Pr_c = 1$, $Ra|Le - 1| \approx 6509$.

Figure 8 shows that, for $Pr < Pr_c$ and the chosen values of the Lewis number, the location of the first supercritical saddle node SN_2 can be approximated by

$$Ra_{SN_2} \approx \frac{6460}{|Le - 1|} \left(\frac{Pr}{Pr_c} \right)^{-0.24}. \tag{4.2}$$

For $Pr < 10^{-2}$ (not shown), the location of saddle node SN_2 deviates from the relation above, indicating a potentially different asymptotic regime. These results also illustrate the large Pr behaviour of the subcritical saddle node SN_1: $Ra_{SN_1}|Le - 1|$ tends to a constant as the Prandtl number tends to infinity. This constant increases with Le and saturates for

https://doi.org/10.1017/jfm.2021.1121 Published online by Cambridge University Press

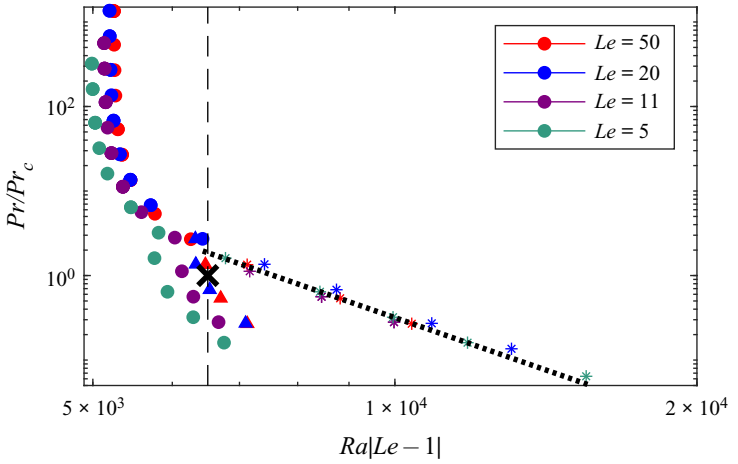


Figure 8. Saddle-node locations for $Le = 5$ (green), $Le = 11$ (purple), $Le = 20$ (blue) and $Le = 50$ (red). The black dashed line marks the location of the primary bifurcation and the black cross marks the codimension two point where the criticality of the primary bifurcation changes, at $Pr = Pr_c$. The black dotted line represents the relationship (4.2). Saddle nodes are marked by circles for SN_1, asterisks for SN_2 and triangles for SN_3.

large values of the Lewis number. These results echo those obtained in doubly diffusive convection in a two-dimensional vertical porous enclosure, where Mamou, Vasseur & Bilgen (1998) used a parallel flow approximation to demonstrate that the Rayleigh number at which the subcritical saddle node occurs is proportional to $1/(1 - Le)$ for large enough Lewis numbers.

4.2. *Solution profiles*

Despite the different scenarios obtained at different values of the Prandtl number (see figure 5), the steady convection states undergo similar structural changes along their branch, as evidenced in figure 9 for $Le = 11$ and $Pr = 1$, 0.032, 0.01 and 0.005. The streamfunction profiles are similar near the primary bifurcation regardless of the value of the Prandtl number (see second column of figure 9), which is in agreement with the linear stability results from figure 3(*c*). Moving along the branches in the direction of increasing energy, the first change that we observe is the strengthening of the anticlockwise roll, where fluid near the hotter wall moves upwards. This occurs in both the subcritical and the supercritical regimes, as can be seen in the third column of figure 9. Continuing the branches to the large-amplitude saddle node and beyond, the amplitude of the weaker roll decreases, leaving room for the stronger roll to straighten. At large enough amplitude, an anticlockwise roll occupies the domain, irrespective of the value of Pr. Its amplitude grows as the upper branch is followed to larger values of Ra, where the Prandtl number starts to impact the flow: the roll occupies a smaller area at lower values of the Prandtl number, as seen within the final column of figure 9. This resembles the fly-wheel convection, with nearly circular streamlines, seen in low Prandtl Rayleigh–Bénard convection as studied by Clever & Busse (1981).

To characterise these observations in more detail, figure 10 reports the horizontal velocity profiles observed on the upper branch for $Pr = 1$, 0.1, 0.032 and 0.005. The decrease in roll size is apparent when Pr is decreased. This is particularly evident for $Pr = 0.005$, where the horizontal velocity remains small except within the range $0.6 \lesssim z \lesssim 1.9$, in such a way that the roll only occupies about half of the domain's extent.

https://doi.org/10.1017/jfm.2021.1121 Published online by Cambridge University Press

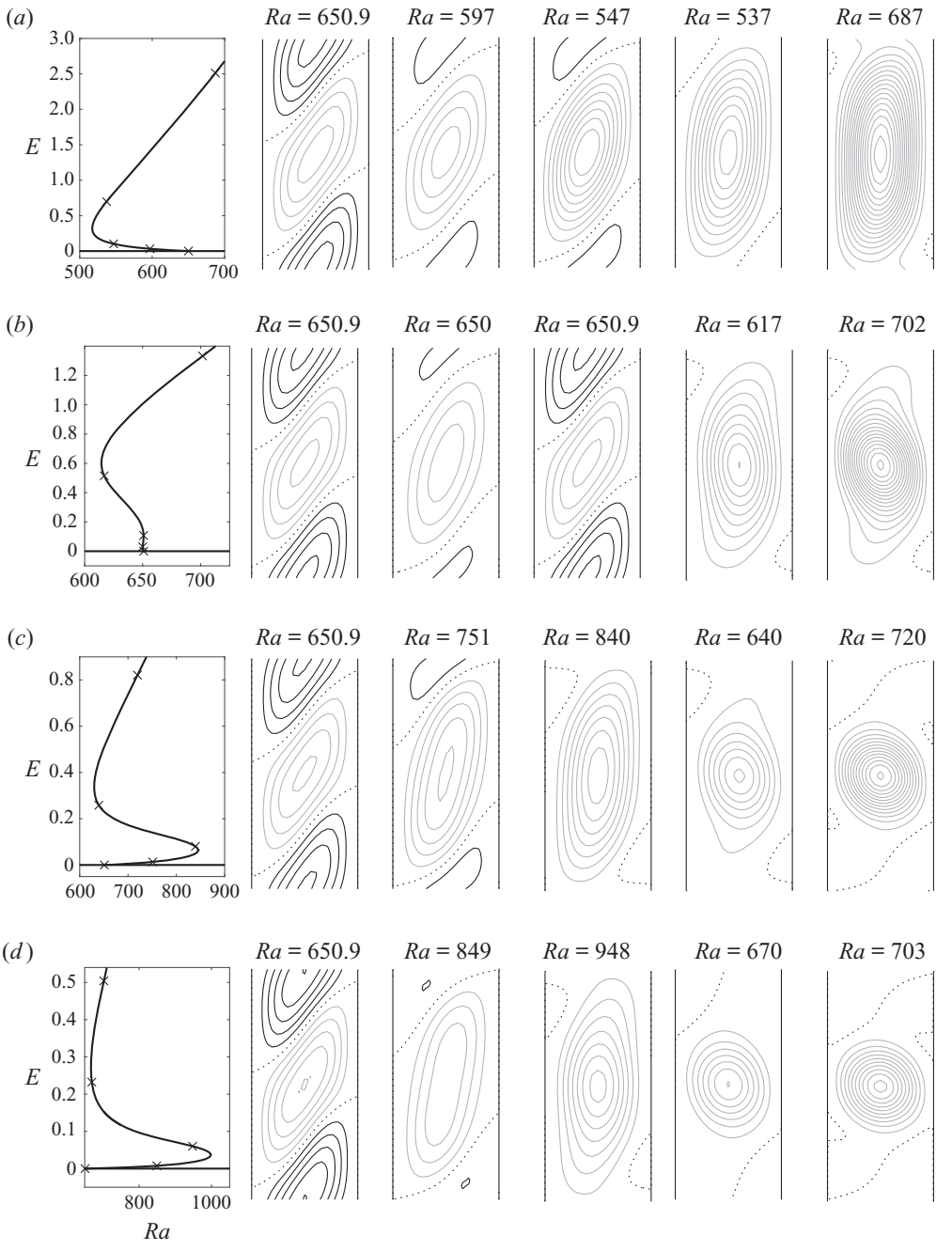


Figure 9. Streamfunctions of the steady states on the primary branch when $Le = 11$ for different values of the Prandtl number: top row $Pr = 1$, second row $Pr = 0.032$, third row $Pr = 0.01$ and bottom row $Pr = 0.005$. The left column shows the respective bifurcation diagrams and indicates with a cross the solutions that have been represented in the subsequent panels. Black (grey, dotted) contours indicate positive (negative, zero) values of the streamfunction. Contour intervals: first column, top two rows – 10^{-4}; first column, third row – 10^{-5}; first column, bottom row – 2×10^{-5}; second column, top two rows – 0.02; second column, bottom two rows – 0.01; third column – 0.02; fourth and fifth columns – 0.05.

https://doi.org/10.1017/jfm.2021.1121 Published online by Cambridge University Press

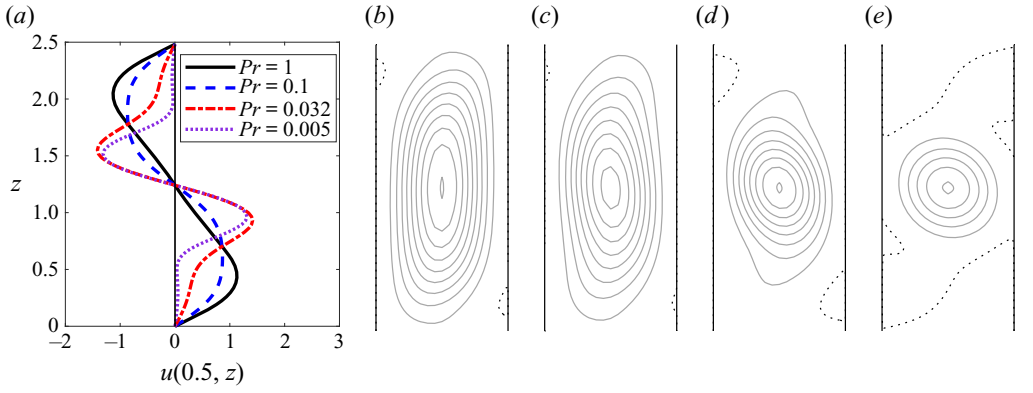


Figure 10. Horizontal velocity and streamfunction of solutions from the upper segment of the primary branch at $Ra = 700$ for $Pr = 1$, 0.1, 0.032, 0.005 and $Le = 11$ represented via (*a*) the midline horizontal velocity ($u(x = 0.5, z)$) and streamfunction contours plots for (*b*) $Pr = 1$, (*c*) $Pr = 0.1$, (*d*) $Pr = 0.032$ and (*e*) $Pr = 0.005$ with contour intervals 0.1.

Figure 10(*a*) additionally shows the transition to these states from the large rolls observed at $O(1)$ Prandtl numbers. For $Pr = 1$, the maximum horizontal velocity is achieved far from the centre of the roll, at $z \approx 0.44,\ 2.04$, producing a region of strong shear between the rolls and gentle quasi-linear velocity variations inside the rolls. As Pr is lowered, these maxima move towards the centre of the roll by initially becoming less pronounced and creating flatter extrema (see figure 10*c*), followed by the emergence of peaks at $z = 1$ and $z \approx 1.5$. The maximum horizontal velocity does not change significantly within this range of Prandtl number values in such a way that the low Pr rolls represent narrow regions of strong shear surrounded by low-amplitude flow.

4.3. *Stability of the nonlinear states*

The stability of states on the primary branch is controlled by two eigenmodes: an amplitude mode that preserves the S_Δ symmetry of the system and a drift mode that breaks the S_Δ symmetry. The translation mode, associated with vertical translations due to the symmetry T_δ, remains marginal along the branch and none of the other eigenmodes become destabilising over the range of parameters considered.

Close to the onset of convection, the amplitude mode is initially destabilising when the bifurcation is subcritical ($Pr > Pr_c$), whereas it is stabilising when the bifurcation is supercritical ($Pr < Pr_c$). This mode subsequently changes stability at successive saddle nodes. In particular, it becomes stabilising at saddle nodes SN_1 and SN_3, where the branch turns towards higher Ra, but becomes destabilising at SN_2, where the branch turns towards lower Ra. As a result, the upper branches of steady convection states are always stable to amplitude perturbations for all Le and Pr.

The drift mode is stabilising near the primary bifurcation at $Ra = Ra_c$ for all Pr, but becomes destabilising at a drift-pitchfork bifurcation further along the branch at $Ra = Ra_d$, whose location depends upon both Le and Pr, as can be seen in figure 7. The marginal mode is identical to the translation mode at this bifurcation and its destabilisation leads to a pair of branches of travelling wave solutions, as shown in figure 11(*a*) for $Pr = 0.1$ and $Le = 11$. Close to their onset, these states take the form of a single large-amplitude convection roll (see figure 11*c*) that slowly drifts either upwards or downwards. As these branches are followed beyond the drift bifurcation, an asymmetric streaming flow

https://doi.org/10.1017/jfm.2021.1121 Published online by Cambridge University Press

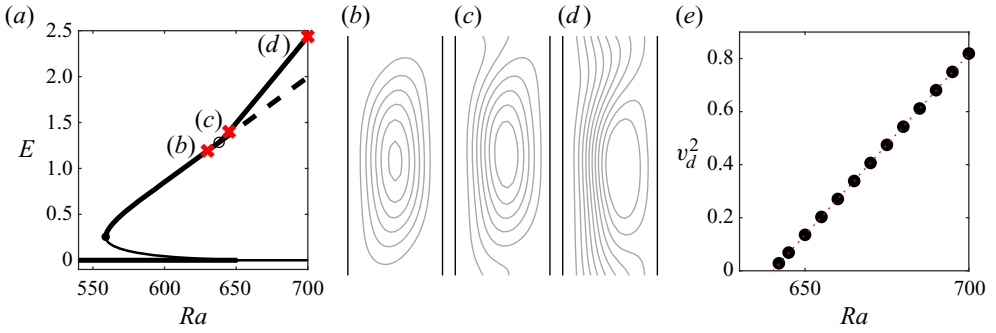


Figure 11. Drift bifurcation and downward-travelling waves for $Pr = 0.1$, $Le = 11$, for which $Ra_d \approx 638$. (*a*) Bifurcation diagram showing the kinetic energy E as a function of the Rayleigh number Ra for steady states and travelling waves. Thick lines indicate stable solutions, thin lines indicate solutions unstable to amplitude perturbations and dashed lines indicate solutions unstable to drift. The drift bifurcation is shown by the open circle. (*b*) Stable convection state at $Ra = 630$ shown by contours of its streamfunction with intervals 0.1 (first red cross in (*a*)). Further panels show similar representations of stable travelling waves at: (*c*) $Ra = 645$ and (*d*) $Ra = 700$. (*e*) Squared drift speed along the stable branch as a function of the Rayleigh number. The dotted line shows the fitting law: $v_d \approx 0.12\sqrt{Ra - 640}$.

strengthens while the convection roll weakens and moves toward the wall where the streaming flow is the weakest. This transition is shown from figure 11(*b*) at $Ra = 630$ to figure 11(*d*) at $Ra = 700$. At the same time, the drift speed increases at a rate approximately proportional to $\sqrt{Ra - Ra_d}$, as shown in figure 11(*e*). This result extends the findings obtained for $Le = 1.2$, $Pr = 1$ by Xin *et al.* (1998) to a wider range of parameter values.

The stability of the travelling waves is determined by the location of the drift bifurcation: these states are initially stable when the bifurcation occurs on the upper branch of steady convection states, whereas they are unstable when the bifurcation occurs along the lower branch. Both cases can be achieved for a given Le when Pr is varied, as figure 7 illustrates for selected values of the Prandtl number with $Le = 11$ and $Le = 20$. For large values of the Prandtl number, the drift bifurcation occurs on the upper branch at large Rayleigh numbers. This location moves closer to the saddle node with decreasing Prandtl numbers so that the two coincide at $Pr = Pr^*$ and $Ra = Ra^*$. For $Le = 11$, we found that $Pr^* \approx 0.042$ and $Ra^* \approx 614.9$ (see figure 7(*c*) for a bifurcation diagram at similar values of the parameters). For smaller values of the Prandtl number, the drift bifurcation occurs along the lower branch of convection states and at a value of the Rayleigh number that increases as Pr is decreased. For all the parameter values tested, this bifurcation was found to occur at larger amplitude than saddle node SN_2 and, consequently, the small-amplitude steady convection states remain stable to drift.

4.4. *Dynamical attractors*

The temporal dynamics of the system changes as the drift bifurcation passes below the subcritical saddle node since all the steady convection states from the upper branch and the travelling wave states are destabilised in the process. Many initial conditions will consequently decay towards the conduction state at low Pr and Ra. This decay is not possible when the conduction state is unstable for $Ra > Ra_c$, where we find that the dynamics converge on time-dependent states.

To understand how this behaviour arises, we unfold the saddle-node-pitchfork normal form near the codimension two point (Ra^*, Pr^*) where the drift bifurcation and saddle

https://doi.org/10.1017/jfm.2021.1121 Published online by Cambridge University Press

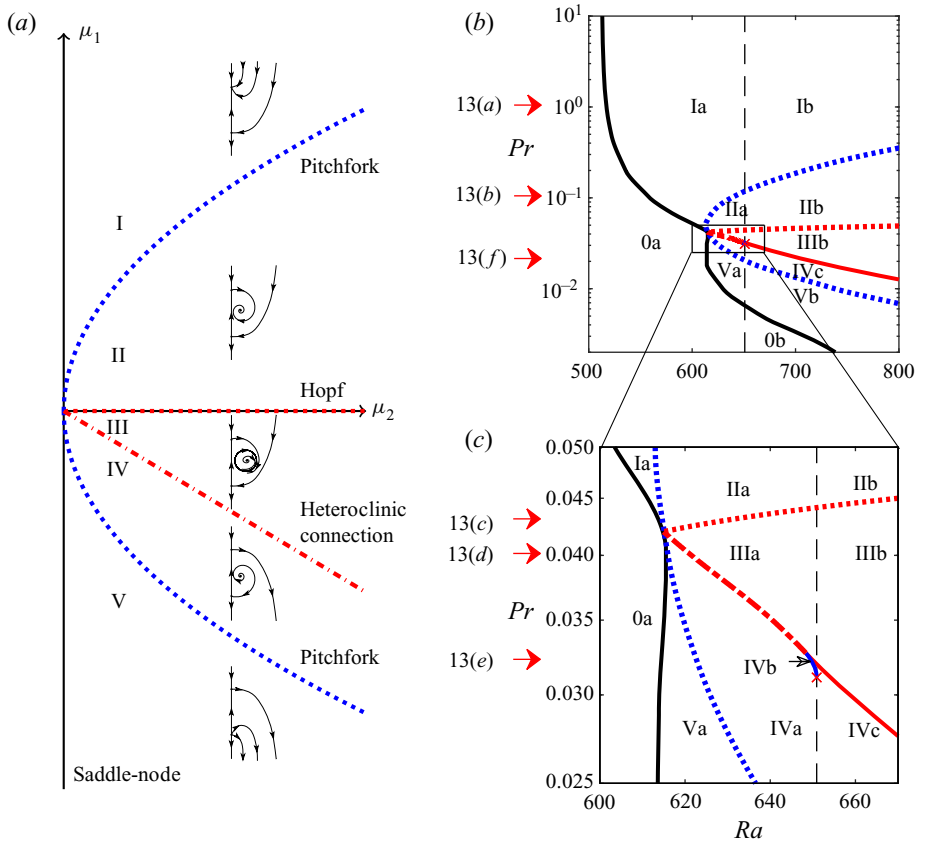


Figure 12. (*a*) Unfolding near the codimension two saddle-node-pitchfork bifurcation at $\mu_1 = \mu_2 = 0$ given by system (4.3), (4.4), after Guckenheimer & Holmes (1983). The different phase portraits are classified in five different regions labelled using Roman numerals and accompanied with a sketch of the corresponding phase space. In each of these sketches, the fixed points on the vertical line represent steady convection states. The vertical (respectively horizontal) direction is the eigendirection related to the amplitude (respectively drift) mode. (*b*) Analogy with the doubly diffusive convection problem is made by replacing μ_1 by $Pr - Pr^*$ and μ_2 by $Ra - Ra^*$ and regions of the (Ra, Pr) parameter space are shown as a function of the observed temporal behaviour for $Le = 11$. (*c*) Magnification of panel (*b*) near (Ra^*, Pr^*). Arrows indicate the values of Pr used to produce the bifurcation diagrams in figure 13. In the panels, the bifurcations are represented by: black, red and blue solid lines (saddle nodes), blue dotted lines (drift bifurcation), red dotted lines (Hopf bifurcation), red dot-dashed lines (heteroclinic connection) and in (*b*,*c*), the vertical dashed lines (primary stationary bifurcation of the conduction state).

node coincide. This unfolding takes the form (Guckenheimer & Holmes 1983)

$$\dot{x} = -\mu_1 x + b_1 xz, \tag{4.3}$$

$$\dot{z} = \mu_2 - x^2 - z^2 + b_2 z^3, \tag{4.4}$$

where x represents the extent to which the state drifts, z represents the amplitude of the convection states, $b_1 > 0$, $b_2 < 0$, and μ_1 and μ_2 are two unfolding parameters that are introduced to respectively represent the deviations $Pr - Pr^*$ and $Ra - Ra^*$.

When $\mu_1 = \mu_2 = 0$, the trivial state, $(x, z) = (0, 0)$, undergoes a codimension two bifurcation. One of five phase portraits is observed in the vicinity of this bifurcation and these are shown in figure 12(*a*). In addition to the steady states previously discussed, the

https://doi.org/10.1017/jfm.2021.1121 Published online by Cambridge University Press

	Stable in region?												
State	Oa	Ob	Ia	Ib	IIa	IIb	IIIa	IIIb	IVa	IVb	IVc	Va	Vb
O	x	—	x	—	x	—	x	—	x	x	—	x	—
SOC_s	—	x	—	—	—	—	—	—	—	x	x	—	x
SOC_l	—	—	x	x	—	—	—	—	—	—	—	—	—
TW	—	—	—	—	x	x	—	—	—	—	—	—	—
PO	—	—	—	—	—	—	x	x	—	—	—	—	—

Table 3. Stability of the observed doubly diffusive states within each region of the parameter space from figure 12. The naming convention used is as follows: O, conduction state; SOC_s, small-amplitude stationary overturning convection; SOC_l, large-amplitude stationary overturning convection; TW, travelling wave; and PO, relative periodic orbit. The regions Oa, . . . , Vb refer to the regions introduced in figure 12.

unfolding reveals the presence of periodic orbits. Relating the unfolding back to doubly diffusive convection, these correspond to relative periodic orbits consisting of drifting states that originate either from a travelling wave undergoing a Hopf bifurcation or from a global bifurcation where two steady convection states connect heteroclinically.

Although the normal form (4.3), (4.4) only formally represents the dynamics of the full system close to the codimension two point, each of the regions shown in figure 12 continues to be observed an appreciable distance away from this point. Figures 12(b) and 12(c) illustrate the extent of the corresponding regions in the doubly diffusive system when $Le = 11$ and we anticipate that similar results will hold for other values of the Lewis number. In this figure, the regions have been subdivided according to the types of stable attracting states that they display. The subdivisions occur owing to the instability of the conduction state at Ra_c and the creation of a pair of saddle nodes at (Ra_{cusp}, Pr_{cusp}), which enrich the previous unfolding. The resulting subregions, together with their associated attracting states, are summarised in table 3 and on the bifurcation diagrams in figure 13. As Pr varies, the system admits one of seven qualitatively distinct bifurcation diagrams. Six of these are presented in figure 13, which also indicate the range of kinetic energies over each relative periodic orbit attained via time stepping. The seventh type of bifurcation diagram, where the primary branch lies entirely within the supercritical regime, is not shown but possesses similar features to that seen for $Pr = 0.02$ in figure 13(f) including stable small-amplitude steady convection states and relative periodic orbits.

The three most relevant stable attracting states close to the primary bifurcation at high Pr ($Pr > Pr^*$ here) are: the conduction state (O), the large-amplitude steady convection states (SOC_l) and the travelling wave states (TW). Below the onset of convection (region Oa), all initial conditions decay towards the first of these. In region Ia, above subcritical onset but before the drift instability, initial conditions converge towards SOC_l, as evidenced by the energy–time and drift speed–time plot in figure 14(a). Increasing Ra beyond the drift instability into region IIa, SOC_l is now unstable and the flow converges towards TW. Figure 14(b) shows that the former state may still be observed in the temporal dynamics as the initial condition first rapidly changes amplitude to approach SOC_l before it builds vertical drift and converges to TW.

The stable branch of travelling waves destabilises in a supercritical Hopf bifurcation that leads to a stable relative periodic orbit, as shown in figure 13 for $Pr = 0.043$. Figures 15(a)–15(e) depict such an orbit shortly after the bifurcation at $Ra = 650$ and $Pr = 0.043$, where we see that the states exhibit small oscillations about a drifting state. The Hopf bifurcation moves towards lower Rayleigh numbers as Pr approaches Pr^* from above, which reduces the extent over which stable TW are found. This continues until

https://doi.org/10.1017/jfm.2021.1121 Published online by Cambridge University Press

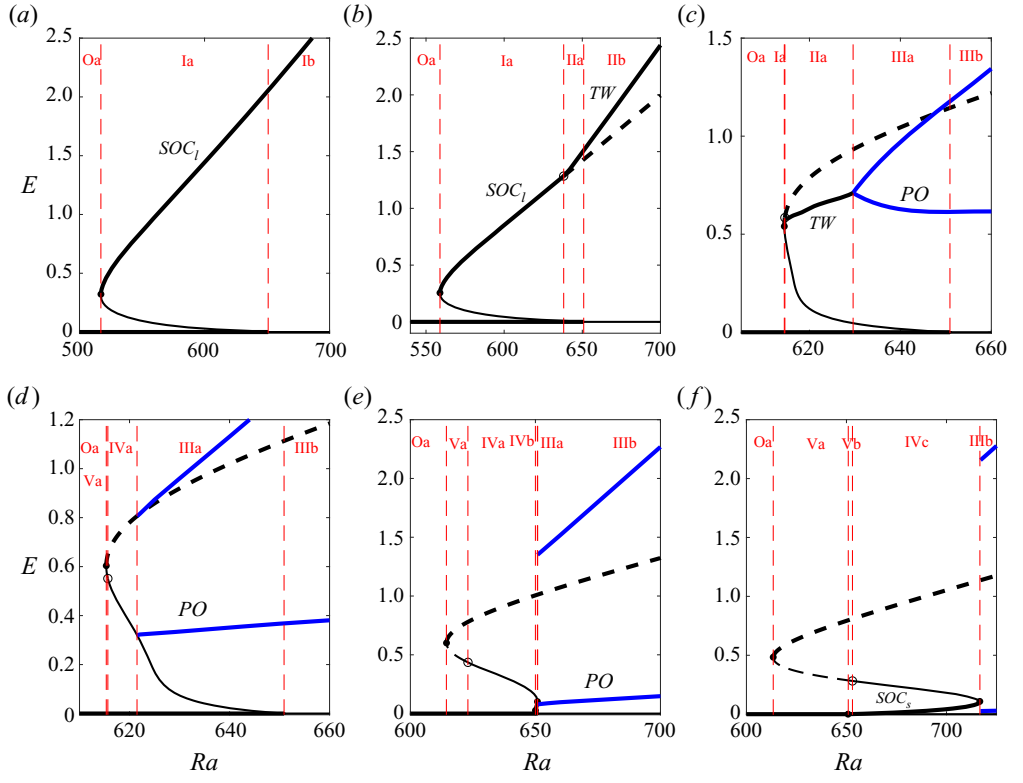


Figure 13. Bifurcation diagrams showing the primary branch and other stable attracting states for $Le = 11$, and (*a*) $Pr = 1$, (*b*) $Pr = 0.1$, (*c*) $Pr = 0.043$, (*d*) $Pr = 0.04$, (*e*) $Pr = 0.032$ and (*f*) $Pr = 0.02$. The solid circles mark the saddle nodes and open circles indicate where the drift bifurcation occurs. Thick (thin) lines represent states stable (unstable) to the amplitude mode whilst solid (dashed) lines show those stable (unstable) to the drift mode. Thick blue lines indicate the minimal and maximal energies achieved in the stable limit cycle, which starts in a Hopf bifurcation in (*c*) and in a heteroclinic bifurcation in (*d–f*). The unstable branches of travelling waves are not shown.

$Pr = Pr^*$, when stable *TW* cease to exist and the relative periodic orbit bifurcates directly from the codimension two bifurcation at the saddle node.

Upon further decreasing of the Prandtl number, so that the drift bifurcation occurs on the lower branch of steady convection, the system admits neither stable SOC_l nor stable *TW*. Instead, the bifurcation diagrams are similar to that shown for $Pr = 0.04$ in figure 13(*d*), where a branch of unstable *TW* extends from the drift bifurcation towards higher Rayleigh numbers and stable relative periodic orbits exist after a global bifurcation, where the stable manifold of SOC_l connects heteroclinically with the unstable manifold of the convection state on the lower branch and vice versa.

The lack of stability of the nonlinear states before the heteroclinic connection lead all initial conditions to decay down to the conduction state in regions IVa and Va. Figures 14(*d*) and 14(*f*) illustrate this tendency for $Pr = 0.032$ when $Ra = 630$ and $Ra = 620$, respectively. In both cases, the amplitude of the initially imposed roll rapidly decreases to approach that of SOC_l rolls. Afterwards, the drift speed of the state increases, as SOC_l is unstable to drift, and reaches a maximum around $t \approx 50$. The drift speed subsequently decays down to zero, due to the instability of *TW*, and the time-dependent state converges on the conduction state, which is the only stable attractor in these regions.

https://doi.org/10.1017/jfm.2021.1121 Published online by Cambridge University Press

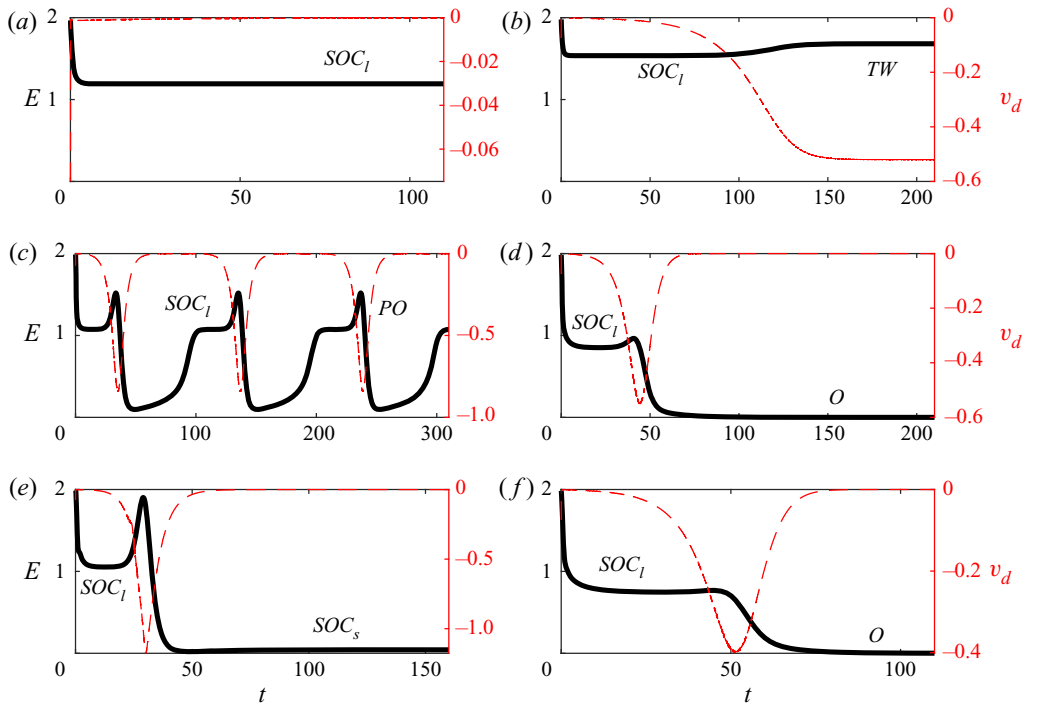


Figure 14. Energy–time (black) and drift speed–time (red) plots illustrating regions I–V in figure 12 with $Le = 11$. In each case, the initial state was the large-amplitude convection state at $Ra = 700$ for $Pr = 0.1$ that was perturbed in the direction of its unstable drift eigenmode. States approached during the trajectory are labelled as follows: (*a*) region Ia, convergence to SOC_l when $Pr = 0.1$ and $Ra = 630$; (*b*) region IIb, convergence to TW when $Pr = 0.1$ and $Ra = 660$; (*c*) region IIIb, convergence to PO when $Pr = 0.032$ and $Ra = 660$, (*d*) region IVa, convergence to O when $Pr = 0.032$ and $Ra = 630$; (*e*) region IVc, convergence to SOC_s when $Pr = 0.02$ and $Ra = 700$; and (*f*) region Va, convergence to O when $Pr = 0.032$ and $Ra = 620$.

Beyond the heteroclinic connection, initial conditions tend to converge towards the relative periodic orbit, as they invariably do in region IIIb, where the conduction state is unstable. Figure 14(*c*) illustrates this convergence starting from a large-amplitude roll with $Pr = 0.032$ and $Ra = 660$ perturbed in the direction of its unstable drift eigenmode. A single cycle of this orbit is shown in further detail in figures 15(*f*)–15(*j*). This relative periodic orbit cycles between the three states: SOC_l, TW and a steady small-amplitude convection state, in the following manner. The first stage of the orbit, from $15 \lesssim t \lesssim 40$, resembles the temporal behaviour seen in region IIa (figure 14*b*), where the solution remains close to SOC_l in profile (figure 15*h*) while the drift speed slowly increases in magnitude. Following this, between $t \approx 40$ and $t \approx 54$, the drift speed and kinetic energy rapidly increase as the profile of the state exhibits properties of the travelling wave (TW) solution (figure 15*i*). Between $t \approx 54$ and $t \approx 68$, both the drift speed and kinetic energy decrease as the state approaches a small-amplitude, non-drifting convection state with inclined rolls (figure 15*j*). The final stage of this orbit is the transition from the small-amplitude back to large-amplitude steady convection, which is indicated by the monotonic increase in kinetic energy while maintaining $v_d \approx 0$ for $t \gtrsim 70$ and $t \lesssim 15$ in figure 15(*g*).

The heteroclinic connection leading to these orbits moves towards higher Rayleigh numbers as Pr decreases and coincides with SN_2 for $Pr \lesssim 0.032$ (see figure 13*e*,*f*).

https://doi.org/10.1017/jfm.2021.1121 Published online by Cambridge University Press

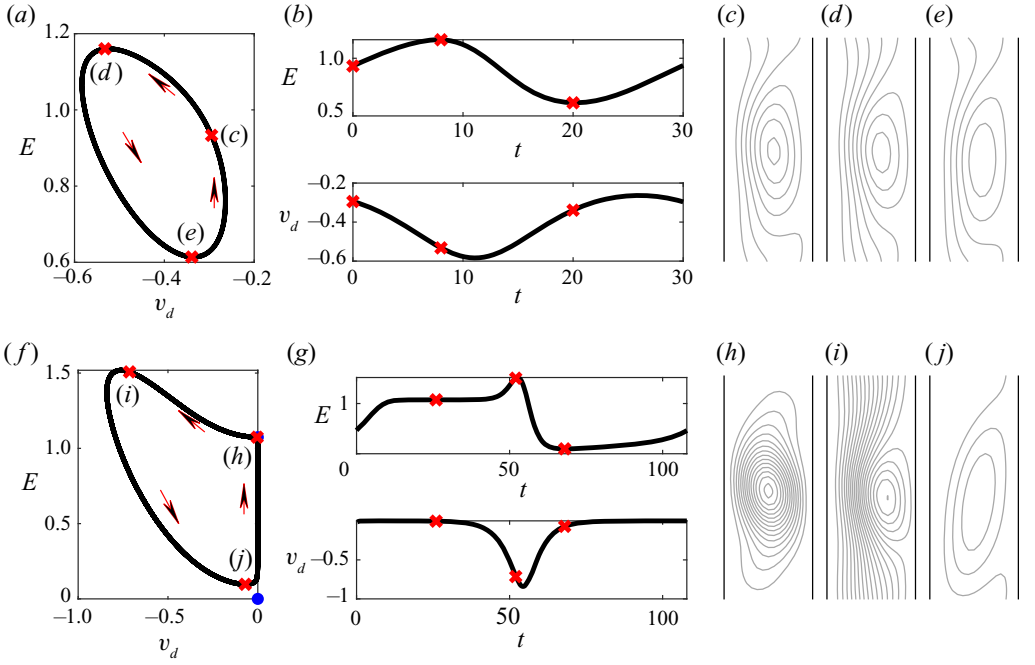


Figure 15. Temporal evolution of downward-travelling states across one cycle of two relative periodic orbits at: (*a–e*) $Ra = 650$ with $Pr = 0.043$ and $Le = 11$ and (*f–j*) $Ra = 660$ with $Pr = 0.032$ and $Le = 11$ (as in figure 14*c*). (*a*,*f*) Anticlockwise trajectory of the periodic orbit in drift speed–energy phase space. Blue dots in (*f*) mark the conduction and steady convection states. (*b*,*g*) Energy–time (top) and drift speed–time (bottom) plots. (*c–e*) Streamfunctions of states along the orbit in (*a*) at (*c*) $t = 0$, (*d*) $t = 8$ and (*e*) $t = 20$ with contour intervals 0.1. (*h–j*) Streamfunctions of states along the orbit in (*f*) at (*h*) $t = 26$, (*i*) $t = 52$ and (*j*) $t = 68$, with contour intervals 0.05. The streamfunctions have been translated vertically for better visual representation.

This suggests that a saddle-node infinite period (SNIPER) bifurcation explains the origin of the relative periodic orbits at low Prandtl and high Rayleigh numbers. However, by considering various properties of the relative periodic orbits for $Pr = 0.032$ and $Le = 11$ as Ra approaches Ra_{SN_2} from above (figure 16), we additionally find that a gluing bifurcation occurs in the vicinity of the SNIPER bifurcation.

At large Rayleigh numbers, a pair of relative periodic orbits with states drifting either upwards or downwards are related by the reflection symmetry. The maximal energy and drift speed attained along these orbits decrease with decreasing Rayleigh number, and the trajectories approach the stable and unstable manifolds of SOC_l, as seen in figure 16(*a*). This leads to the two relative periodic orbits connecting in a gluing bifurcation around $Ra \approx 652$ so that the trajectories become a single periodic orbit where states alternately drift in opposite directions. This is reminiscent of the pulsating waves seen in nonlinear magnetoconvection (Matthews *et al.* 1993).

The resulting single periodic orbit persists until Ra_{SN_2}, where it terminates in the SNIPER bifurcation. This is evidenced by the period of a single loop of the orbit scaling like $t_P \propto (Ra - Ra_{SN_2})^{-0.56}$ as SN_2 is approached, which is close to the expected $t_P \approx |Ra - Ra_{SN_2}|^{-0.5}$ scaling. The energy–time plots in figure 16(*c*) illustrate that the predominant increase in duration occurs near the small-amplitude steady convection state as the orbit approaches the steady state at SN_2 in phase space. We also find that the time spent near SOC_l increases, whilst the time where the state has large drift speed remains

https://doi.org/10.1017/jfm.2021.1121 Published online by Cambridge University Press

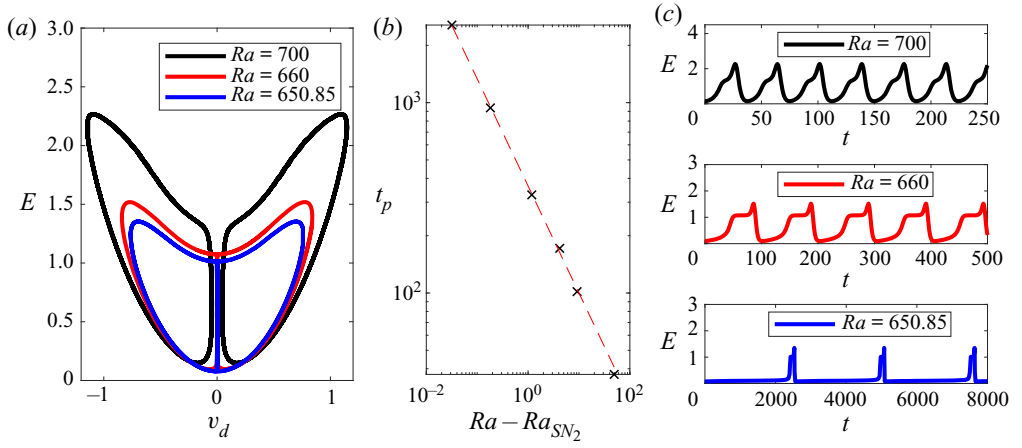


Figure 16. Relative periodic orbits for $Le = 11$, $Pr = 0.032$ where $Ra_{SN_2} \approx 650.82$. (*a*) Trajectories in (v_d, E) phase space for $Ra = 650.85$ (blue), $Ra = 660$ (red) and $Ra = 700$ (black). For $Ra = 700$ and $Ra = 660$, a pair of relative periodic orbits associated with either negative or positive drift velocity are shown, while for $Ra = 650.85$, a single periodic orbit with alternating negative and positive drift velocities is shown. (*b*) Period t_P of orbits for selected $Ra > Ra_{SN_2}$. The red dashed line shows that approximately $t_P \propto (Ra - Ra_{SN_2})^{-0.56}$. (*c*) Energy–time plots for $Ra = 700$ (top), $Ra = 660$ (middle) and $Ra = 650.85$ (bottom).

small, implying that the global bifurcation is due to the collision of the periodic orbit with the stable manifold of SOC_l.

The final attracting state that the flow may converge to is SOC_s, as figure 14(*e*) illustrates for $Pr = 0.02$ and $Ra = 700$. This is possible for $Pr < Pr_{cusp}$ in the supercritical regions Ob, IVc and Vb, where it is the only stable attracting state, and in the subcritical region IVb, where convergence towards the stable conduction state is also possible.

5. Discussion

This paper considers doubly diffusive convection driven by horizontal gradients of temperature and concentration, a configuration typically referred to as natural doubly diffusive convection. We have extended the linear stability analysis of Ghorayeb & Mojtabi (1997) by performing a thorough weakly nonlinear analysis of the system. This was complemented by a numerical exploration of the nonlinear regime, thereby also extending the analysis of Xin *et al.* (1998), who focused on $Pr = 1$ and $Le = 1.2$. From this analysis, we unravelled the relationships between saddle nodes, drift and global bifurcations.

We have identified regions where the resulting primary branch exhibits qualitatively different behaviour. For large values of the Prandtl number, the bifurcation is subcritical and hysteresis takes place between the conduction state and large-amplitude convection. Whereas, for Prandtl numbers below a critical value, the primary bifurcation is supercritical but this is preceded by the creation of two saddle nodes without affecting the existence of large-amplitude convection. Despite this, we did not find any hysteresis in the supercritical regime owing to the presence of a destabilising drift bifurcation along the primary branch. The presence of multiple folds along a primary supercritical branch has already been observed in a non-homogeneous fluid system (Erenburg *et al.* 2003) but we believe that is the first time that it has been observed in homogeneously forced convection in such a small domain.

https://doi.org/10.1017/jfm.2021.1121 Published online by Cambridge University Press

By determining the stability of steady convection states along the primary branch, we identified a codimension two point between a large-amplitude saddle node and a drift bifurcation. We analysed the dynamics around this codimension two point using its normal form and numerical simulations to investigate new Hopf and heteroclinic bifurcations giving rise to periodic orbits. Such time-dependent states are common features of low Prandtl number doubly diffusive convection (see also Umbría & Net 2019). Finally, we provided a classification of the various regions in (Ra, Pr) parameter space according to the nature of their dynamical attractors, for a representative value of the Lewis number.

We anticipate that the analysis provided in this paper may serve as a guide for future research in natural doubly diffusive convection by providing a comprehensive map of the near-onset dynamics as a function of the parameter values. Despite our attempt to be thorough, the characterisation of the nonlinear regime at very small Prandtl numbers, which is relevant in astrophysical contexts (see Garaud 2018), remains to be explored. We observed that this regime behaves differently from extrapolated predictions from $O(1)$ Prandtl numbers but have not pursued this any further.

Lastly, the coexistence of steady overturning convection with the stable conduction state when the primary bifurcation is supercritical has important dynamical implications, which will be the subject of future exploration. In particular, it makes this system a candidate for spatially localised pattern formation in a supercritical fluid system, owing to the similarity of the primary branch structure with the Swift–Hohenberg equation considered by Knobloch, Uecker & Wetzel (2019).

Funding. This work was supported by the Leeds–York Natural Environment Research Council (NERC) Doctoral Training Partnership (DTP) SPHERES under grant NE/L002574/1 and undertaken on ARC3, part of the High Performance Computing facilities at the University of Leeds, UK.

Declaration of interests. The authors report no conflict of interest.

Author ORCIDs.
Cédric Beaume https://orcid.org/0000-0003-3485-6387;
Alastair M. Rucklidge https://orcid.org/0000-0003-2985-0976.

Appendix A. Further expressions for the weakly nonlinear analysis

A.1. *Second-order corrections*

The solution to the system at $O(\epsilon^2)$ (3.14) given in (3.26) involves parameter-free functions $\tilde{u}_i, \tilde{w}_i, \tilde{p}_i$ and $\tilde{\theta}_i$ for $i = 2, \ldots, 7$ within the expressions for $\boldsymbol{\Psi}_2^0$, $\boldsymbol{\Psi}_2^1$ and $\boldsymbol{\Psi}_2^2$ (3.27)–(3.29). These functions satisfy the forced linear equations

$$\begin{pmatrix} -D & 0 & 0 & 0 \\ 0 & D^2 & 0 & 0 \\ 0 & 0 & D^2 & Ra_c(1-Le) \\ 0 & 0 & 0 & D^2 \end{pmatrix} \begin{pmatrix} \tilde{p}_2 \\ \tilde{w}_2 \\ \tilde{w}_3 \\ \tilde{\theta}_3 \end{pmatrix} = \begin{pmatrix} f_{10} \\ f_{20} \\ 0 \\ f_{40} \end{pmatrix}, \tag{A1}$$

$$\begin{pmatrix} D^2-4k_c^2 & 0 & -D & 0 \\ 0 & D^2-4k_c^2 & -2\mathrm{i}k_c & Ra_c(1-Le) \\ D & 2\mathrm{i}k_c & 0 & 0 \\ -1 & 0 & 0 & D^2-4k_c^2 \end{pmatrix} \begin{pmatrix} \tilde{u}_4 \\ \tilde{w}_4 \\ \tilde{p}_4 \\ \tilde{\theta}_4 \end{pmatrix} = \begin{pmatrix} f_{12} \\ f_{22} \\ 0 \\ 0 \end{pmatrix}, \tag{A2}$$

https://doi.org/10.1017/jfm.2021.1121 Published online by Cambridge University Press

$$\begin{pmatrix} D^2-4k_c^2 & 0 & -D & 0 & 0 \\ 0 & D^2-4k_c^2 & -2\mathrm{i}k_c & Ra_c(1-Le) & 0 \\ D & 2\mathrm{i}k_c & 0 & 0 & 0 \\ -1 & 0 & 0 & D^2-4k_c^2 & 0 \\ -1 & 0 & 0 & 0 & D^2-4k_c^2 \end{pmatrix} \begin{pmatrix} \tilde{u}_5 \\ \tilde{w}_5 \\ \tilde{p}_5 \\ \tilde{\theta}_5 \\ \tilde{\theta}_6 \end{pmatrix} = \begin{pmatrix} 0 \\ 0 \\ 0 \\ f_{42} \\ 0 \end{pmatrix}, \tag{A3}$$

$$\begin{pmatrix} D^2-k_c^2 & 0 & -D & 0 \\ 0 & D^2-k_c^2 & -\mathrm{i}k_c & Ra_c(1-Le) \\ D & \mathrm{i}k_c & 0 & 0 \\ -1 & 0 & 0 & D^2-k_c^2 \end{pmatrix} \begin{pmatrix} \tilde{u}_7 \\ \tilde{w}_7 \\ \tilde{p}_7 \\ \tilde{\theta}_7 \end{pmatrix} = \begin{pmatrix} f_{11} \\ f_{21} \\ f_{31} \\ f_{41} \end{pmatrix}, \tag{A4}$$

where $D = \mathrm{d}/\mathrm{d}x$, and $\tilde{u}_i$, $\tilde{w}_i$ and $\tilde{\theta}_i$ satisfy homogeneous boundary conditions and the pressure boundary conditions come from a projection of the Navier–Stokes equation onto the sidewalls

$$\tilde{u}_i = 0, \quad \tilde{w}_i = 0, \quad -\frac{\partial \tilde{p}_i}{\partial x} + \frac{\partial^2 \tilde{u}_i}{\partial x^2} = 0, \quad \tilde{\theta}_i = 0 \quad \text{on } x = 0, 1. \tag{A5}$$

A.2. *Coefficients in the Ginzburg–Landau equation*

Expressions for the coefficients α, β, γ and δ in the Ginzburg–Landau equation (3.33) are obtained by evaluating

$$\begin{aligned} \alpha &= \frac{1}{Pr}\Big(\langle U^\dagger, U_1\rangle + \langle W^\dagger, W_1\rangle\Big) + (1+Le)\langle \Theta^\dagger, \Theta_1\rangle \\ &= \frac{1}{Pr}\alpha_1 + (1+Le)\alpha_2, \end{aligned} \tag{A6}$$

$$\begin{aligned} \beta &= -\left(\frac{1}{Pr}\langle U^\dagger, \mathcal{N}_3^U\rangle + \frac{1}{Pr}\langle W^\dagger, \mathcal{N}_3^W\rangle + \frac{1}{1-Le}\langle \Theta^\dagger, \mathcal{N}_3^\Theta - Le\mathcal{N}_3^\Phi\rangle\right) \\ &= \frac{1}{Pr^2}\beta_1 + \frac{1+Le}{Pr}\beta_2 + (1+Le^2)\beta_3 + Le\beta_4, \end{aligned} \tag{A7}$$

$$\begin{aligned} \gamma &= (1-Le)\langle W^\dagger, \Theta_1\rangle \\ &= (1-Le)\gamma_1, \end{aligned} \tag{A8}$$

$$\begin{aligned} \delta &= \langle U^\dagger, U_1\rangle + \langle W^\dagger, W_1\rangle + \langle \Theta^\dagger, \Theta_1\rangle \\ &\quad + 2\mathrm{i}k_c\Big(\langle U^\dagger, \tilde{u}_7\rangle + \langle W^\dagger, \tilde{w}_7\rangle + \langle \Theta^\dagger, \tilde{\theta}_7\rangle\Big) + \langle P^\dagger, \tilde{w}_7\rangle - \langle W^\dagger, \tilde{p}_7\rangle, \end{aligned} \tag{A9}$$

where the nonlinear functions $\mathcal{N}_3^F$, for $F = U, W, \Theta, \Phi$, and coefficients β_i for $i = 1, 2, 3, 4$ are

$$\mathcal{N}_3^F = U_1\frac{\mathrm{d}F_2^0}{\mathrm{d}x} + \bar{U}_1\frac{\mathrm{d}F_2^2}{\mathrm{d}x} + U_2^2\frac{\mathrm{d}\bar{F}_1}{\mathrm{d}x} + 2\mathrm{i}k_c\bar{W}_1F_2^2 + \mathrm{i}k_cW_2^0F_1 - \mathrm{i}k_cW_2^2\bar{F}_1, \tag{A10}$$

$$\begin{aligned} \beta_1 = &-\left\langle U^\dagger, \bar{U}_1\frac{\mathrm{d}\tilde{u}_4}{\mathrm{d}x} + \tilde{u}_4\frac{\mathrm{d}\bar{U}_1}{\mathrm{d}x} + 2\mathrm{i}k_c\tilde{u}_4\bar{W}_1 + \mathrm{i}k_c\tilde{w}_2U_1 - \mathrm{i}k_c\tilde{w}_4\bar{U}_1\right\rangle \\ &-\left\langle W^\dagger, U_1\frac{\mathrm{d}\tilde{w}_2}{\mathrm{d}x} + \bar{U}_1\frac{\mathrm{d}\tilde{w}_4}{\mathrm{d}x} + \tilde{u}_4\frac{\mathrm{d}\bar{W}_1}{\mathrm{d}x} + \mathrm{i}k_c\bar{W}_1\tilde{w}_4 + \mathrm{i}k_cW_1\tilde{w}_2\right\rangle, \end{aligned} \tag{A11}$$

https://doi.org/10.1017/jfm.2021.1121 Published online by Cambridge University Press

α_1	1.11×10^{-4}	β_2	-1.63×10^{-8}	$(Le > 1)\ \gamma_1$	-8.85×10^{-7}
α_2	2.27×10^{-4}	β_3	7.47×10^{-8}	$(Le < 1)\ \gamma_1$	8.85×10^{-7}
β_1	-4.43×10^{-9}	β_4	1.58×10^{-7}	δ	7.38×10^{-4}

Table 4. Numerical values of the coefficients α_1, α_2, β_1, β_2, β_3, β_4, γ_1 and δ in (3.33). The sign of γ_1 depends upon whether $Le > 1$ or $Le < 1$ as $\gamma > 0$ for all Le, while all other coefficients are independent of the parameters Le and Pr.

$$\beta_2 = -\left\langle U^\dagger, \bar{U}_1 \frac{\mathrm{d}\tilde{u}_5}{\mathrm{d}x} + \tilde{u}_5 \frac{\mathrm{d}\bar{U}_1}{\mathrm{d}x} + 2\mathrm{i}k_c \tilde{u}_5 \bar{W}_1 + \mathrm{i}k_c \tilde{w}_3 U_1 - \mathrm{i}k_c \tilde{w}_5 \bar{U}_1 \right\rangle$$
$$- \left\langle W^\dagger, U_1 \frac{\mathrm{d}\tilde{w}_3}{\mathrm{d}x} + \bar{U}_1 \frac{\mathrm{d}\tilde{w}_5}{\mathrm{d}x} + \tilde{u}_5 \frac{\mathrm{d}\bar{W}_1}{\mathrm{d}x} + \mathrm{i}k_c \bar{W}_1 \tilde{w}_5 + \mathrm{i}k_c W_1 \tilde{w}_3 \right\rangle$$
$$- \left\langle \Theta^\dagger, \bar{U}_1 \frac{\mathrm{d}\tilde{\theta}_4}{\mathrm{d}x} + \tilde{u}_4 \frac{\mathrm{d}\bar{\Theta}_1}{\mathrm{d}x} + 2\mathrm{i}k_c \bar{W}_1 \tilde{\theta}_4 + \mathrm{i}k_c \tilde{w}_2 \Theta_1 - \mathrm{i}k_c \tilde{w}_4 \bar{\Theta}_1 \right\rangle, \tag{A12}$$

$$\beta_3 = -\left\langle \Theta^\dagger, U_1 \frac{\mathrm{d}\tilde{\theta}_3}{\mathrm{d}x} + \bar{U}_1 \frac{\mathrm{d}\tilde{\theta}_5}{\mathrm{d}x} + \tilde{u}_5 \frac{\mathrm{d}\bar{\Theta}_1}{\mathrm{d}x} + 2\mathrm{i}k_c \bar{W}_1 \tilde{\theta}_5 + \mathrm{i}k_c \tilde{w}_3 \Theta_1 - \mathrm{i}k_c \tilde{w}_5 \bar{\Theta}_1 \right\rangle, \tag{A13}$$

$$\beta_4 = -\left\langle \Theta^\dagger, U_1 \frac{\mathrm{d}\tilde{\theta}_3}{\mathrm{d}x} + \bar{U}_1 \left(\frac{\mathrm{d}\tilde{\theta}_5}{\mathrm{d}x} + \frac{\mathrm{d}\tilde{\theta}_6}{\mathrm{d}x} \right) + 2\tilde{u}_5 \frac{\mathrm{d}\bar{\Theta}_1}{\mathrm{d}x} \right.$$
$$\left. + 2\mathrm{i}k_c \left(\bar{W}_1 \left(\tilde{\theta}_5 + \tilde{\theta}_6 \right) + \tilde{w}_3 \Theta_1 - \tilde{w}_5 \bar{\Theta}_1 \right) \right\rangle. \tag{A14}$$

These expressions for the parameter-free coefficients α_i, β_i, γ_1 and δ are evaluated numerically and are given in table 4.

Of particular interest is the boundary where the primary bifurcation changes from subcritical to supercritical. This occurs when $\beta = 0$, which we may find explicitly by taking the positive root of (A7), to find

$$Pr_c = \frac{-(1+Le)\beta_2 + \sqrt{(1+Le)^2\beta_2^2 - 4\beta_1\left[(1+Le^2)\beta_3 + Le\beta_4\right]}}{2[(1+Le^2)\beta_3 + Le\beta_4]}. \tag{A15}$$

A.3. *Effect of thermal and solution advective terms on a_2*

To determine the contributions that each of the nonlinear terms make to a_2, we introduce the factors ζ_1 and ζ_2 that multiply the thermal and solutal advective terms, respectively. We numerically perform the weakly nonlinear analysis for the modified system

$$\frac{1}{Pr}\left(\frac{\partial \boldsymbol{u}}{\partial t} + \boldsymbol{u}\cdot\boldsymbol{\nabla}\boldsymbol{u}\right) = -\boldsymbol{\nabla}p + \nabla^2\boldsymbol{u} + Ra(T-C)\hat{\boldsymbol{z}}, \tag{A16}$$

$$\boldsymbol{\nabla}\cdot\boldsymbol{u} = 0, \tag{A17}$$

https://doi.org/10.1017/jfm.2021.1121 Published online by Cambridge University Press

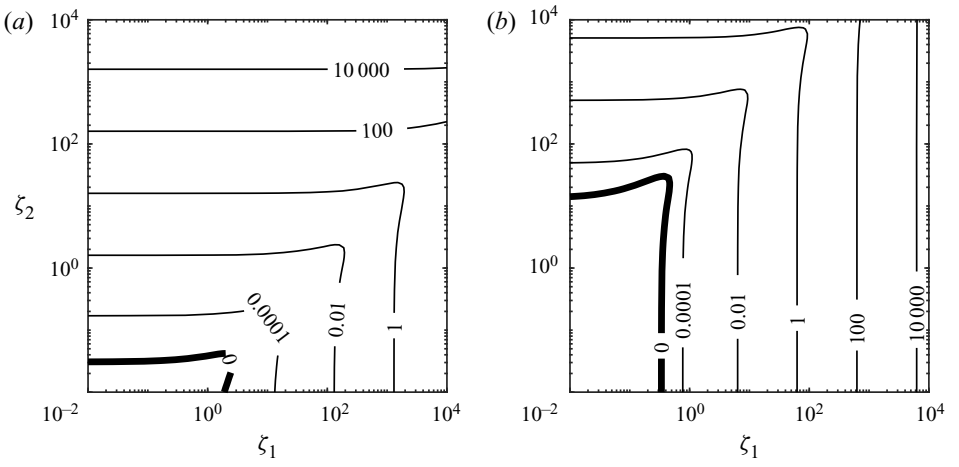


Figure 17. Contours of the coefficient a_2 as a function of ζ_1 and ζ_2, which respectively multiply thermal and solutal advective nonlinearities in (A16)–(A19), for (*a*) $Le = 11$, $Pr = 1$ and (*b*) $Le = 1/11$, $Pr = 1$. The contour $a_2 = 0$, which marks the boundary between subcriticality and supercriticality, is shown in bold.

$$\frac{\partial T}{\partial t} + \zeta_1 \boldsymbol{u} \cdot \boldsymbol{\nabla} T = \nabla^2 T, \tag{A18}$$

$$\frac{\partial C}{\partial t} + \zeta_2 \boldsymbol{u} \cdot \boldsymbol{\nabla} C = \frac{1}{Le} \nabla^2 C, \tag{A19}$$

with ζ_1, $\zeta_2 \in [10^{-2}, 10^4]$ and selected values of the Prandtl and Lewis numbers. The coefficient a_2 tends to increase when one of ζ_1 or ζ_2 increases, while keeping the other fixed, as indicated by the contours in figure 17. Thus, advection of both heat and solute enhance the subcriticality of the primary bifurcation.

References

Batiste, O., Knobloch, E., Mercader, I. & Net, M. 2001 Simulations of oscillatory binary fluid convection in large aspect ratio containers. *Phys. Rev.* E **65**, 016303.

Beaume, C. 2017 Adaptive Stokes preconditioning for steady incompressible flows. *Commun. Comput. Phys.* **22** (2), 494–516.

Beaume, C. 2020 Transition to doubly diffusive chaos. *Phys. Rev. Fluids* **5** (10), 103903.

Beaume, C., Bergeon, A. & Knobloch, E. 2011 Homoclinic snaking of localized states in doubly diffusive convection. *Phys. Fluids* **23**, 094102.

Beaume, C., Bergeon, A. & Knobloch, E. 2013*a* Convectons and secondary snaking in three-dimensional natural doubly diffusive convection. *Phys. Fluids* **25** (2), 024105.

Beaume, C., Bergeon, A. & Knobloch, E. 2013*b* Nonsnaking doubly diffusive convectons and the twist instability. *Phys. Fluids* **25**, 114102.

Beaume, C., Bergeon, A. & Knobloch, E. 2018 Three-dimensional doubly diffusive convectons: instability and transition to complex dynamics. *J. Fluid Mech.* **840**, 74–105.

Bergeon, A., Ghorayeb, K. & Mojtabi, A. 1999 Double diffusive convection in an inclined cavity. *Phys. Fluids* **11**, 549–559.

Bergeon, A. & Knobloch, E. 2002 Natural doubly diffusive convection in three-dimensional enclosures. *Phys. Fluids* **14** (9), 3233–3250.

Bergeon, A. & Knobloch, E. 2008*a* Periodic and localized states in natural doubly diffusive convection. *Physica* D **237** (8), 1139–1150.

Bergeon, A. & Knobloch, E. 2008*b* Spatially localized states in natural doubly diffusive convection. *Phys. Fluids* **20** (3), 034102.

Bethe, H.A. 1990 Supernova mechanisms. *Rev. Mod. Phys.* **62**, 801–866.

https://doi.org/10.1017/jfm.2021.1121 Published online by Cambridge University Press

CLEVER, R.M. & BUSSE, F.H. 1981 Low-Prandtl-number convection in a layer heated from below. *J. Fluid Mech.* **102**, 61–74.

CROSS, M.C., DANIELS, P.G., HOHENBERG, P.C. & SIGGIA, E.D. 1983 Phase-winding solutions in a finite container above the convective threshold. *J. Fluid Mech.* **127**, 155–183.

DEANE, A.E., KNOBLOCH, E. & TOOMRE, J. 1988 Traveling waves in large-aspect-ratio thermosolutal convection. *Phys. Rev.* A **37**, 1817–1820.

DIJKSTRA, H.A. & KRANENBORG, E.J. 1996 A bifurcation study of double diffusive flows in a laterally heated stably stratified liquid layer. *Intl J. Heat Mass Transfer* **39** (13), 2699–2710.

ERENBURG, V., GELFGAT, A.Y., KIT, E., BAR-YOSEPH, P.Z. & SOLAN, A. 2003 Multiple states, stability and bifurcations of natural convection in a rectangular cavity with partially heated vertical walls. *J. Fluid Mech.* **492**, 63–89.

GARAUD, P. 2018 Double-diffusive convection at low Prandtl number. *Annu. Rev. Fluid Mech.* **50**, 275–298.

GHORAYEB, K. & MOJTABI, A. 1997 Double diffusive convection in a vertical rectangular cavity. *Phys. Fluids* **9** (8), 2339–2348.

GUCKENHEIMER, J. & HOLMES, P. 1983 *Nonlinear Oscillations, Dynamical Systems and Bifurcations of Vector Fields*. Springer.

HUPPERT, H.E. & SPARKS, R.S.J. 1984 Double diffusive convection due to crystallization in magmas. *Annu. Rev. Earth Planet Sci.* **12**, 11–37.

HUPPERT, H.E. & TURNER, J.S. 1981 Double-diffusive convection. *J. Fluid Mech.* **106**, 299–329.

KARNIADAKIS, G.E., ISRAELI, M. & ORSZAG, S.A. 1991 High-order splitting methods for the incompressible Navier–Stokes equations. *J. Comput. Phys.* **97** (2), 414–443.

KELLEY, D.E., FERNANDO, H.J.S., GARGETT, A.E., TANNY, J. & ÖZSOY, E. 2003 The diffusive regime of double diffusive convection. *Prog. Oceanogr.* **56**, 461–481.

KNOBLOCH, E. 2015 Spatial localization in dissipative systems. *Annu. Rev. Condens. Matter Phys.* **6**, 325–359.

KNOBLOCH, E., MOORE, D.R., TOOMRE, J. & WEISS, N.O. 1986 Transitions to chaos in two-dimensional double-diffusive convection. *J. Fluid Mech.* **166**, 409–448.

KNOBLOCH, E., UECKER, H. & WETZEL, D. 2019 Defectlike structures and localized patterns in the cubic-quintic-septic Swift–Hohenberg equation. *Phys. Rev.* E **100** (1), 012204.

KOLODNER, P. 1991 Stable and unstable pulses of traveling-wave convection. *Phys. Rev.* A **43**, 2827–2832.

KRISHNAMURTI, R. 2003 Double-diffusive transport in laboratory thermohaline staircases. *J. Fluid Mech.* **483**, 287–314.

KRISHNAMURTI, R. 2009 Heat, salt and momentum transport in a laboratory thermohaline staircase. *J. Fluid Mech.* **638**, 491–506.

LAY, T., HERNLUND, J. & BUFFETT, B.A. 2008 Core–mantle boundary heat flow. *Nat. Geosci.* **1**, 25–32.

MAMOU, M., VASSEUR, P. & BILGEN, E. 1998 Double-diffusive convection instability in a vertical porous enclosure. *J. Fluid Mech.* **368**, 263–289.

MAMUN, C.K. & TUCKERMAN, L.S. 1995 Asymmetry and Hopf bifurcation in spherical Couette flow. *Phys. Fluids* **7** (1), 80–91.

MATTHEWS, P.C., PROCTOR, M.R.E., RUCKLIDGE, A.M. & WEISS, N.O. 1993 Pulsating waves in nonlinear magnetoconvection. *Phys. Lett.* A **183** (1), 69–75.

MERCADER, I., BATISTE, O., ALONSO, A. & KNOBLOCH, E. 2009 Localized pinning states in closed containers: homoclinic snaking without bistability. *Phys. Rev.* E **80**, 025201.

MERCADER, I., BATISTE, O., ALONSO, A. & KNOBLOCH, E. 2011 Convectons, anticonvectons and multiconvectons in binary fluid convection. *J. Fluid Mech.* **667**, 586–606.

PALIWAL, R.C. & CHEN, C.F. 1980*a* Double-diffusive instability in an inclined fluid layer. Part 1. Experimental investigation. *J. Fluid Mech.* **98**, 755–768.

PALIWAL, R.C. & CHEN, C.F. 1980*b* Double-diffusive instability in an inclined fluid layer. Part 2. Stability analysis. *J. Fluid Mech.* **98**, 769–785.

PÉREZ-SANTOS, I., GARCÉS-VARGAS, J., SCHNEIDER, W., ROSS, L., PARRA, S. & VALLE-LEVINSON, A. 2014 Double-diffusive layering and mixing in patagonian fjords. *Prog. Oceanogr.* **129**, 35–49.

PREDTECHENSKY, A.A., MCCORMICH, W.D., SWIFT, J.B., NOSZTICZIUS, Z. & SWINNEY, H.L. 1994 Onset of traveling waves in isothermal double diffusive convection. *Phys. Rev. Lett.* **72**, 218–221.

REQUILÉ, Y., HIRATA, S.C., OUARZAZI, M.N. & BARLETTA, A. 2020 Weakly nonlinear analysis of viscous dissipation thermal instability in plane Poiseuille and plane Couette flows. *J. Fluid Mech.* **886**, A26.

RUCKLIDGE, A.M. 1992 Chaos in models of double convection. *J. Fluid Mech.* **237**, 209–229.

SCHMITT, R.W. 1983 The characteristics of salt fingers in a variety of fluid systems, including stellar interiors, liquid metals, oceans, and magmas. *Phys. Fluids* **26** (9), 2373–2377.

SCHMITT, R.W. 1994 Double diffusion in oceanography. *Annu. Rev. Fluid Mech.* **26**, 255–285.

https://doi.org/10.1017/jfm.2021.1121 Published online by Cambridge University Press

SCHMITT, R.W., LEDWELL, J.R., MONTGOMERY, E.T., POLZIN, K.L. & TOOLE, J.M. 2005 Enhanced diapycnal mixing by salt fingers in the thermocline of the tropical Atlantic. *Science* **308** (5722), 685–688.
SCHMITT, R.W., PERKINS, H., BOYD, J.D. & STALCUP, M.C. 1987 C-SALT: an investigation of the thermohaline staircase in the western tropical North Atlantic. *Deep-Sea Res.* **34** (10), 1655–1665.
SHANKAR, B.M., KUMAR, J. & SHIVAKUMARA, I.S. 2021 Stability of double-diffusive natural convection in a vertical fluid layer. *Phys. Fluids* **33** (9), 094113.
SPIEGEL, E.A. 1969 Semiconvection. *Comments on Astrophysics and Space Physics*, 1–57.
SPIEGEL, E.A. 1972 Convection in stars II. Special effects. *Annu. Rev. Astron. Astrophys.* **10**, 261–304.
SPINA, A., TOOMRE, J. & KNOBLOCH, E. 1998 Confined states in large-aspect-ratio thermosolutal convection. *Phys. Rev.* E **57**, 524–547.
TSITVERBLIT, N. 1995 Bifurcation phenomena in confined thermosolutal convection with lateral heating: commencement of the double-diffusive region. *Phys. Fluids* **7** (4), 718–736.
TSITVERBLIT, N. & KIT, E. 1993 The multiplicity of steady flows in confined double-diffusive convection with lateral heating. *Phys. Fluids* A **5** (4), 1062–1064.
UMBRÍA, J.S. & NET, M. 2019 Stationary flows and periodic dynamics of binary mixtures in tall laterally heated slots. In *Computational Modelling of Bifurcations and Instabilities in Fluid Dynamics* (ed. A. Gelfgat), pp. 171–216. Springer.
WATANABE, T., IIMA, M. & NISHIURA, Y. 2012 Spontaneous formation of travelling localized structures and their asymptotic behaviour in binary fluid convection. *J. Fluid Mech.* **712**, 219–243.
WATANABE, T., IIMA, M. & NISHIURA, Y. 2016 A skeleton of collision dynamics: hierarchical network structure among even-symmetric steady pulses in binary fluid convection. *SIAM J. Appl. Dyn. Syst.* **15**, 789–806.
WILCOX, W.R. 1993 Transport phenomena in crystal growth from solution. *Prog. Cryst. Growth Charact. Mater.* **26**, 153–194.
XIN, S., LE QUÉRÉ, P. & TUCKERMAN, L.S. 1998 Bifurcation analysis of double-diffusive convection with opposing horizontal thermal and solutal gradients. *Phys. Fluids* **10** (4), 850–858.
YOU, Y. 2002 A global ocean climatological atlas of the turner angle: implications for double-diffusion and water-mass structure. *Deep-Sea Res.* **49**, 2075–2093.

https://doi.org/10.1017/jfm.2021.1121 Published online by Cambridge University Press